

To appear in *The Astrophysical Journal*, September 2000

Aluminum Abundances, Deep Mixing and the Blue-Tail Second-Parameter Effect in the Globular Clusters M 3 and M 13

Robert M. Cavallo^{1,2}

Laboratory for Astronomy and Solar Physics, NASA/Goddard Space Flight Center, Greenbelt, MD 20771

rob@shemesh.gsfc.nasa.gov

and

Neil M. Nagar¹

Department of Astronomy, University of Maryland, College Park, MD 20742

ABSTRACT

We analyze high resolution, high signal-to-noise spectra of six red-giant-branch (RGB) stars in the globular cluster M 3 (NGC 5272) and three in M 13 (NGC 6205) that were obtained with the Mayall 4-meter telescope and echelle spectrometer on Kitt Peak. The spectra include lines of O, Na, Mg, Al, Si, Ca, Ti, V, Mn, Fe and Ni. We also analyze the [Al/Fe] values of 96 RGB stars in M 13 covering the brightest 3.5 magnitudes, which include 66 measurements that were derived from moderate resolution, low signal-to-noise spectra obtained with the WIYN 3.5-meter telescope and Hydra multi-object spectrograph, also on Kitt Peak. In addition, we compile from the literature and inspect the [Na/Fe] values of 119 RGB stars in M 13. We test for bimodality in the [Al/Fe] and [Na/Fe] distributions using the KMM algorithm and find that the [Al/Fe] values in M 13 are distributed bimodally at all points along the RGB that were observed, while the [Na/Fe] values are bimodal only over the brightest two magnitudes. The ratios of Al-enhanced to Al-normal and Na-enhanced to Na-normal giants increase towards the tip of the RGB in M 13, which is suggestive of deep mixing in this cluster. The limited M 3 data exhibit a bimodal distribution of [Al/Fe] values and are suggestive of no deep mixing; however, they are too few to be conclusive. We further test for a relationship between deep mixing on the RGB and a second parameter that can create the extended blue tail seen along the horizontal-branches of some clusters by using an “instantaneous” mixing algorithm, which we develop here. We

¹Visiting Astronomer, Kitt Peak National Observatory. KPNO is operated by AURA, Inc. under contract to the National Science Foundation.

²NRC Research Associate

conclude that the data for both clusters are consistent with deep mixing as a “blue-tail second parameter”, and we suggest future observations to further constrain the results. Finally, we offer a solution to the problem of over producing sodium during deep mixing that is based on the depletion of ^{22}Ne in asymptotic-giant-branch stars and suggest that pollution might best be traced by *s*-process elements in the Sr-Y-Zr peak.

Subject headings: globular clusters: individual (M 3,M 13) — stars: abundances — stars: horizontal branch — stars: late-type — stars: Population II

1. INTRODUCTION

According to canonical stellar evolution models, the by-products of the nuclear processing around the hydrogen-burning shell (H shell) of low-mass red-giant-branch (RGB) stars should remain confined to the stellar interior; however, observations over the past 25 years have shown star-to-star variations in the elements C, N, O, Na, Mg and Al, among others, on the surfaces of globular cluster red giants (see Kraft 1994, Briley et al. 1994 and Cavallo 1998a for detailed reviews of the observations). In particular, the data show evidence of the CNO cycle that dominates the energy production in such stars: C and O are anticorrelated with N, while the $^{12}\text{C}/^{13}\text{C}$ ratio is near the equilibrium value of 4 in many clusters (Suntzeff & Smith 1991; Shetrone 1996b; Briley et al. 1997a,b; Zucker et al. 1996). While the first dredge-up phenomenon (Iben 1967) does alter the carbon and nitrogen abundances slightly, it cannot account for the observed large variations of these elements and their isotopic ratios, nor can it account for the variations of the other elements. In addition, some elements show evidence for gradual changes along the RGB, indicating that something is occurring during the course of evolution to facilitate these alterations. For example, C becomes more depleted with decreasing V in the clusters M 15, M 55, M 92 and NGC 6397 (Bell et al. 1979; Carbon 1982; Trefzger et al. 1983; Briley et al. 1990).

Two separate approaches have been developed to address the observations. One assumes that some form of non-canonical mixing occurs along the RGB, which gradually brings material from around the H shell to the stellar surface (Sweigart & Mengel 1979, hereafter, SM79). Models by SM79, Denisenkov & Denisenkova (1990), Langer et al. (1993), Cavallo et al. (1996), Denissenkov & Weiss (1996) and Cavallo et al. (1998, hereafter, CSB98) have shown that most variations along the brighter part of the RGB can be explained by nuclear processing around the H shell combined with mixing. The source of mixing is generally assumed to be rotationally induced meridional circulation currents (SM79); although, other theories abound (Langer et al. 1997; Fujimoto et al. 1999). The observations by Peterson (1983) that show the horizontal-branch (HB) stars in M 13, a cluster with large variations of oxygen and aluminum on the RGB, rotating nearly a factor of two faster than the HB stars in M 3, a cluster with a composition similar to M 13, but with less extreme abundance variations along its RGB, support the SM79 hypothesis.

The second approach assumes that some of the variations, particularly those of the heavier

elements, are primordial in nature, perhaps originating in the processed envelopes of intermediate-mass asymptotic-giant-branch (AGB) stars that were shed into the nascent cluster environment (Cottrell & Da Costa 1981). While it has been shown that this scenario cannot account for all the variations (Denissenkov et al. 1997), some aspects of it are plausible in light of the data. For example, observations of CN-band strength and sodium variations on the upper main sequence of 47 Tuc, sodium enhancements on the subgiant branch of M 92 and enhancements in the neutron-capture elements in some clusters all point to primordial origins (Briley et al. 1989, 1991; Shetrone 1996a; Briley et al. 1996; Cannon et al. 1998; King et al. 1998; Ivans et al. 1999). The most likely solution to the abundance anomaly problem probably involves a combination of both scenarios, where primordial pollution is present in the cluster, but mixing later plays a role in adjusting the abundance patterns (see, e.g., Denissenkov et al. 1998 and Briley et al. 1999), an approach we examine here.

This paper focuses on determining the chemical abundances in the red giants of the globular clusters M 3 (NGC 5272) and M 13 (NGC 6205) from high resolution, high signal-to-noise echelle spectra obtained with the Mayall 4-meter telescope on Kitt Peak. We choose these two clusters because they are often considered a classical “second-parameter” pair since they have markedly different HB’s, despite having similar $[\text{Fe}/\text{H}]$ ³ values, the first parameter. We discuss the hypothesis that deep mixing along the RGB, which we define as mixing that penetrates the H shell, brings helium to the surface and affects the HB morphology as a second parameter that creates the extended blue tail in M 13 (Sweigart 1997a,b). One oft-quoted choice for the second parameter is a relative age difference between M 3 and M 13 (Fusi Pecci & Bellazini 1997; Sarajedini et al. 1997; Chaboyer et al. 1998); however, this is not borne out by the photometry (Johnson & Bolte 1998; VandenBerg 1999; Grundahl 1999) and leaves open the need for a qualified alternative.

While M 13 is by far the most well-studied cluster for abundance variations, the data for M 3 are lacking. One goal of this paper is to increase our knowledge of the chemical abundances in this latter cluster so that it can be compared with M 13 in greater detail.

The outline of this paper is as follows: we describe the observations, data reduction approach, abundance analysis technique and abundance results in sections 1, 2, 3 and 4, respectively. In section 5 we discuss evidence for and the implications of deep mixing along the RGB, and we give our conclusions in section 6. In the appendix we derive the instantaneous mixing algorithm that is used in section 5.

2. OBSERVATIONS

We chose five bright giants in M 3 (MB 4, vZ 205, vZ 297, vZ 1000 and vZ 1127) and three in M 13 (L 262, L 324 and L 414) from previous studies by the “Lick/Texas” group (Kraft et al.

³We use the usual notation: $[\text{X}/\text{Y}] = \log(\text{X}/\text{Y})_\star - \log(\text{X}/\text{Y})_\odot$.

1992, 1993, 1995) that show evidence for abundance variations but have no information regarding aluminum. The observations were made on the nights of 29-31 May 1998 using the echelle spectrograph on the Mayall 4-meter telescope. The echelle setup used - echelle grating 31.6-63°, cross grating 226-1, long-focus camera and the T2KB CCD - resulted in continuous spectral coverage between 5500 Å and 8800 Å at a dispersion of 0.08 Å per CCD pixel, i.e. resolution, $R \sim 30,000$ at 6000 Å over a 2.5 pixel resolution element. The central wavelength on the CCD was chosen to maximize the signal-to-noise ratio near the $\lambda\lambda 6696, 6698$ Å Al I lines. The seeing was typically between 1" and 1".2 on all three nights, causing us to use a slit-width of 1".5, and a slit length of 7".5. Each 4×30 min. exposure of a target star was sandwiched between two 15 s exposures of a ThAr comparison lamp, which was observed at the same telescope position and slit position angle (P.A.). To facilitate subtraction of telluric lines we observed one or two fast rotating B stars each night at various airmasses.

In addition to our data, Dr. M. Briley provided us with the reduced spectrum of the M 3 giant AA and a fast rotating B star, taken on 21 March 1998 with the McDonald Observatory 2.7-m telescope and 2D-Coude echelle spectrograph. His set-up yielded an non-continuous wavelength coverage from 4070 Å to 10,500 Å with $R \sim 50,000$ over a resolution element.

A log of all the observations with estimates of the signal-to-noise ratio around the $\lambda\lambda 6696, 6698$ Å Al I region is given in Table 1. The photometry is from Ferraro et al. (1997) for M 3 and from Cudworth & Monet (1979) for M 13. The locations of the program stars in their respective color-magnitude diagrams are given in Figure 1 for M 3 and Figure 2 for M 13. In the following discussions, we refer to each star by its most commonly used identification, which in some cases is its alternate name.

3. CCD PROCESSING AND SPECTRA EXTRACTION

The data were reduced using standard IRAF⁴(Tody 1986) tasks (version 2.11.1), following the reduction procedure outlined in “Users guide to reducing Echelle spectra with IRAF”, by D. Wilmarth & J. Barnes⁵. Zero frames were taken on each night, but since $> 99.9\%$ of the pixels had zero values within the 5 e⁻ r.m.s. noise of the T2KB CCD, we only zero-corrected “hot” (zero values > 5 e⁻) pixels. Quartz flat exposures were taken on each of the three nights and used to flat field the target stars and to determine “dead” pixels.

After initial processing of the CCD target star data, we used the IRAF task APSCATTER to correct for scattered light between the orders. The orders were then extracted to single dimensional spectra using the task APSUM with variance weighting, and then wavelength calibrated using the

⁴IRAF is distributed by the National Optical Astronomy Observatories, which are operated by the Association of Universities for Research in Astronomy, Inc., under cooperative agreement with the National Science Foundation.

⁵available by anonymous ftp to <ftp://iraf.noao.edu/iraf/docs>

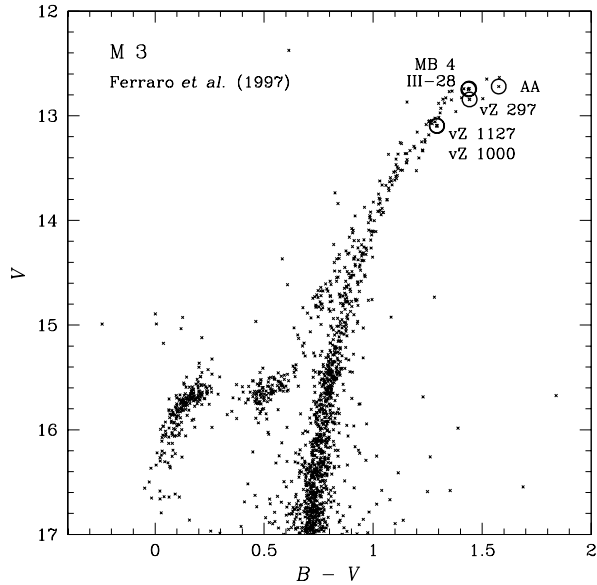


Fig. 1.— Color-magnitude diagram for M 3, with the program stars circled and labeled. The data are from Ferraro et al. (1997).

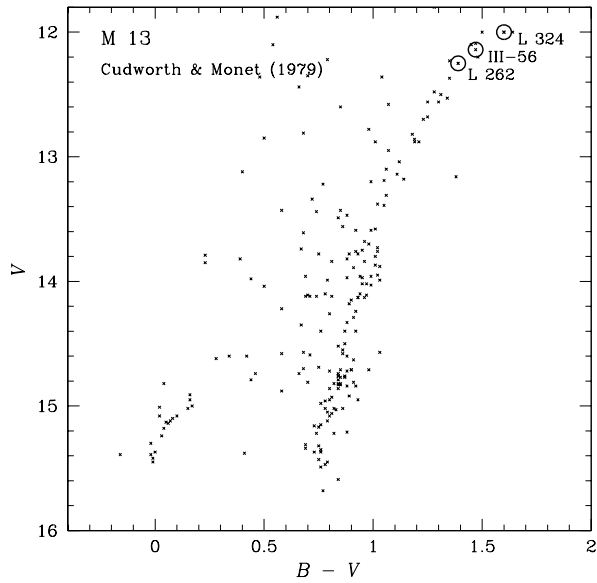


Fig. 2.— As Figure 1, except for M 13 with the data from Cudworth & Monet (1979).

closest (in time) ThAr spectrum, taken at the same telescope position and slit P.A. as the target star. Orders that contained telluric lines were corrected using the task TELLURIC and a comparison spectrum of a fast-rotating B star that was observed at an airmass similar to the program star. Finally, each spectrum was shifted into the rest frame and flattened by fitting a spline through the continuum.

The spectrum for the star M 3 AA was given to us in its extracted form and required only correction for telluric lines in some orders.

Figure 3 shows the spectra around the Al I region for all the M 3 and M 13 giants. The variation in the Al I line strengths is quite apparent from one star to the next.

4. ABUNDANCE ANALYSIS

4.1. Equivalent Widths, Line Lists and Line Parameters

The free spectral range for the Mayall 4-meter data is less than the width of the CCD so that each line appears at least twice in our spectra, with one line usually towards the center of the chip where the noise is minimized. Unfortunately, combining adjacent orders to increase the number of photon counts resulted in a lowered signal-to-noise ratio since the edges of the chip contained much lower quality spectra than the center. We measured the equivalent widths of the line closer to the center of the CCD and present the results in Table 2 (found after REFERENCES). The equivalent widths were determined by summing the flux in a line if the line was cleanly separated from other lines or by fitting a Gaussian in more crowded regions. Some data are excluded from the table for one of several reasons: 1) In the case of M 3 AA, some lines fell between the orders; 2) the line was too weak to be measured (our minimum measurable equivalent width was about 5 mÅ, depending on the signal-to-noise ratio); 3) the line was contaminated by either a bad column or a cosmic ray hit; or 4) in very few cases, the line gave abundance results that were anomalously discordant with the mean and r.m.s. deviation of the rest of the lines of the same species for unknown reasons and was rejected.

4.1.1. *Fe lines*

The iron lines were chosen from Kurucz's CD-ROM # 23⁶ and the solar atlas of Moore et al. (1966). They were used to determine both the iron abundances and the model-atmosphere parameters and were thus selected to have a broad range in excitation potentials and oscillator strengths, which were adopted without modification from the empirically derived tables of Nave et al. (1994) and Biémont et al. (1991) for the Fe I and Fe II lines, respectively. We rejected Fe I

⁶<http://cfa-www.harvard.edu/amdata/ampdata/amdata.html>

Table 1. Observing Log

| Star | Alt. | <i>V</i> mag. | <i>B</i> – <i>V</i> mag. | Date Obs. U.T. | Exposure min. | S/N est. |
|---------|-------------------------|------------------|-----------------------------|-------------------------------|------------------|-------------|
| M 3 | | | | | | |
| vZ 238 | AA, SK 586, F 12959 | 12.72 | 1.58 | 21-23 March 1998 ^a | 180 | 110 |
| vZ 752 | MB 4, F 14194 | 12.74 | 1.44 | 1 June 1998 | 120 | 115 |
| vZ 205 | III-28, SK 617, F 16682 | 12.75 | 1.44 | 31 May 1998 | 120 | 95 |
| vZ 297 | SK 525, F 9 | 12.84 | 1.44 | 30 May 1998 | 120 | 105 |
| vZ 1127 | MB 26, F 14246 | 13.09 | 1.29 | 31 May/1 June 1998 | 180 | 135 |
| vZ 1000 | SK 297, F 17307 | 13.10 | 1.29 | 31 May/1 June 1998 | 180 | 90 |
| M 13 | | | | | | |
| L 324 | V 11, CM 425 | 12.00 | 1.60 | 1 June 1998 | 120 | 160 |
| L 414 | III-56, CM 176 | 12.14 | 1.47 | 30 May 1998 | 120 | 140 |
| L 262 | CM 476 | 12.25 | 1.39 | 31 May 1998 | 120 | 140 |

^aObserved by M. Briley

Note. — Star names taken from the catalogs of von Zeipel (1908, vZ) and Ludendorf (1905, L). Alternate names are from Sandage (1953, AA, III-28), Arp (1955, III-56), Hogg (1973, V11), Cudworth & Monet (1979, CM), Sandage & Karem (1982, SK), Ferraro et al. (1997, F) and Michael Bolte (1998, priv comm. MB).

lines that were listed by Nave et al. (1994) as showing blends with other iron lines or uncertainties in their energy levels of more than 0.005 cm^{-1} . For the sake of comparison, we measured the equivalent widths of our chosen iron lines in the visible and near-infrared solar spectra⁷ of Wallace et al. (1993, 1998)⁸ and folded them through the Holweger & Müller (1974) solar model atmosphere with a microturbulent velocity of 1.0 km s^{-1} . We adjusted the $\log gf$'s to reproduce an assumed solar iron abundance of $\log \epsilon(\text{Fe})_{\odot} = 7.52^9$. This results in an average difference between the two sets of oscillator strengths (in the sense of solar model – laboratory) of $+0.09 \pm 0.12$ for Fe I and $+0.05 \pm 0.08$ for Fe II (see Table 3). Both differences show a slight trend toward lower oscillator strengths from the laboratory measurements ($< 1 \sigma$), which in turn would cause the determined iron abundances to be overestimated by 0.09 and 0.05 dex from the Fe I and Fe II lines, respectively.

4.1.2. EW comparisons

In the main panel of Figure 4 we compare the equivalent widths of our iron lines with those from the earlier Lick/Texas studies. The solid line in the figure has a 45 degree slope and represents perfect agreement between the two data sets. The Lick/Texas data tend toward higher equivalent widths relative to our data, especially above $\sim 100 \text{ m}\text{\AA}$. The average differences between the two data sets (in the sense of Lick/Texas – present work) are $6.9 \pm 9.7 \text{ m}\text{\AA}$ for Fe I and $5.9 \pm 9.7 \text{ m}\text{\AA}$ for Fe II. We attribute the differences to several factors. First, our present data have higher signal-to-noise ratios than the Lick/Texas data (90 to 160 compared with 40 - 100), which reduces the level of uncertainty in placing the continuum. Second, the Lick/Texas spectra have higher resolution, $R \sim 48,000$ compared with $R \sim 30,000$, which helps separate lines from the continuum and other lines. Third, the two datasets were reduced using two separate software packages that apply scattered-light corrections differently (see, e.g., Sneden et al. 1991), which can affect the continuum levels and depths of each line. Fourth, measuring equivalent widths is subjective and two different observers can get different results from the same data. For example, the inset in Figure 4 shows the equivalent widths for two separate observations of the M 13 giant III-56 by the Lick/Texas group and demonstrates how much variability can be present in the data even with consistent reduction techniques (see also Kraft et al. 1993, Figure 1). Fifth, the methods of measuring equivalent widths differ: we use both a Simpson's rule technique (i.e., direct integration) and Gaussian fits, while the Lick/Texas results come from Gaussian fits for their earlier papers and both techniques for Kraft et al. (1997).

⁷NSO/Kitt Peak FTS data used here were produced by NSF/NOAO.

⁸available at <http://www.nso.noao.edu/diglib/ftp.html>

⁹ $\log \epsilon(X) = \log N(X/H) + 12.00$, where N is the number abundance. For an informative debate about the preferred solar iron abundance we refer the reader to the papers of Blackwell et al. (1995a), Holweger et al. (1995), Blackwell et al. (1995b) and Kostik et al. (1996). For consistency with the Lick/Texas studies we adopt the 7.52 value.

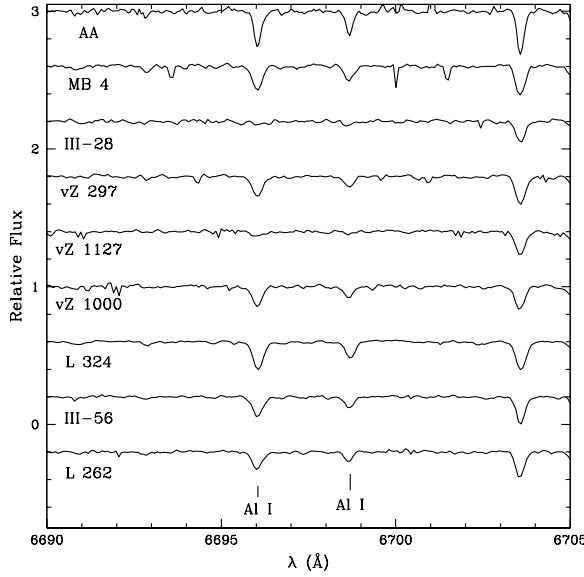


Fig. 3.— The Al I spectral region for all M 3 and M 13 stars observed. The ordinate is in relative units, with each spectrum offset from the others. The Al I lines at $\lambda\lambda 6696, 6698$ Å are labeled.

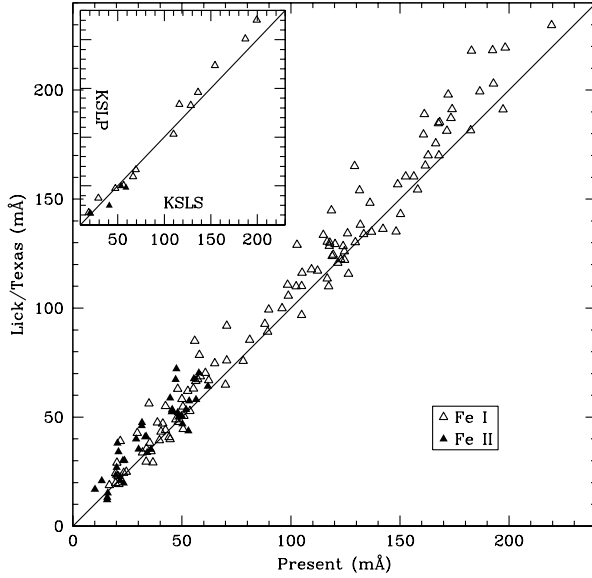


Fig. 4.— Main panel: Our Fe I and Fe II equivalent widths compared with the measurements from the Lick/Texas group. Inset: Comparison of Fe I and Fe II equivalent width measurements for the M 13 giant III-56 from two different studies by the Lick/Texas group [Kraft et al. 1992 (KSLP) and Kraft et al. 1993 (KSLS)]. The scale on the ordinate is identical to the abscissa. The solid line in both plots has a slope of 1.

4.1.3. Other lines

We determined the oscillator strengths for the other elements in our study by measuring the equivalent widths in the solar spectrum and adjusting the $\log gf$ values until we derived the Anders & Grevesse (1989) solar abundances using the Holweger & Müller (1974) solar model. Table 3 lists the average differences between the values we determined and the literature values, which are mostly from Thévenin (1990), who did a similar differential analysis using an older solar spectrum with a MARCS (Gustafsson et al. 1975) solar model and a microturbulent velocity of 0.6 km s^{-1} . With the exception of the Mn I lines, we used our derived $\log gf$'s to derive the elemental abundances. The two Mn I lines in the solar spectrum (we discard a third line at $\lambda 6022 \text{ \AA}$ since it blends with a nearby Fe I feature) suffer from hyperfine splitting effects. To avoid detailed calculations, we adopt the recommended $\log gf$'s from Thévenin (1990) for these two manganese lines.

4.2. Model Parameters: Effective Temperature, Gravity and Microturbulence

4.2.1. Spectroscopic models

We constructed models using the Fe I and Fe II lines with the MARCS model atmosphere code and the MOOG abundance-analysis code (Sneden 1973). The initial models were built with the parameters determined by the Lick/Texas group and were constructed with the alpha elements enhanced by 0.4 dex in accordance with previous observations of cluster giants (see, e.g., Kraft et al. 1997). We iteratively ran MOOG and MARCS to refine the models until the derived abundances were independent of excitation potential, line width and ionization level. We checked our final choice of model parameters by independently using the Ni I lines to determine T_{eff} , the Ni I and Ti I lines to determine the microturbulent velocity, v_t , and the Ti I and Ti II lines to determine $\log g$. The results were generally in agreement with the more numerous iron lines and allowed us to estimate systematic errors in the model parameters determined from spectroscopy: $\Delta T_{\text{eff}} \sim \pm 30 \text{ K}$, $\Delta \log(g) \sim \pm 0.2 \text{ cm s}^{-2}$, and $\Delta v_t \sim \pm 0.15 \text{ km s}^{-1}$.

Our final spectroscopically determined model parameters are given in Table 4, along with the original Lick/Texas model parameters, and are the parameters we used to derive the elemental abundances. The effective temperatures generally agree to less than 100 K, while our gravities are typically lower than the Lick/Texas values by 0.15 ± 0.27 dex and our microturbulent velocities are lower by $0.09 \pm 0.11 \text{ km s}^{-1}$. The differences are consistent with the error estimates derived from the nickel and titanium lines and are not surprising given the differences in the equivalent widths and the choices of lines and line parameters between the two studies.

Table 3. Comparison of Oscillator Strengths

| Species | Avg. | Diff | $\pm\sigma$ | # Lines | Ref. |
|---------|---------------------|--------------------|-------------|----------|------|
| Na I | +0.015 | 0.021 | 2 | T90 | |
| Mg I | +0.263 | 0.349 | 3 | T90, K | |
| Al I | +0.035 | 0.052 | 6 | T90, K | |
| Si I | +0.059 | 0.108 | 9 | T90, K | |
| Ca I | +0.203 | 0.059 | 8 | T90, K | |
| Ti I | -0.025 | 0.113 | 8 | T90, K | |
| Ti II | -0.120 | 0.282 | 2 | T90 | |
| V I | +0.048 | 0.084 | 18 | T89, T90 | |
| Mn I | +0.615 ^a | 0.064 ^a | 2 | T90 | |
| Ni I | +0.203 | 0.097 | 12 | T90 | |
| Fe I | +0.088 | 0.123 | 24 | N | |
| Fe II | +0.048 | 0.077 | 8 | B | |

^aUsed values from Thévenin (1990).

References. — B = Biémont et al. (1991); K = Kurucz CD-ROM #23; N = Nave et al. (1994); T89 = Thévenin (1989); T90 = Thévenin (1990).

Table 4. Spectroscopic Models

| Star | Present Work | | | Lick/Texas | | |
|---------|------------------|----------|-------|------------------|----------|-------|
| | T_{eff} | $\log g$ | v_t | T_{eff} | $\log g$ | v_t |
| M 3 | | | | | | |
| AA | 4050 | 0.40 | 2.27 | 4000 | 0.40 | 2.25 |
| MB 4 | 4060 | 0.45 | 2.05 | 3925 | 0.30 | 2.15 |
| III-28 | 4175 | 0.55 | 1.84 | 4160 | 0.75 | 1.75 |
| vZ 297 | 4050 | 0.25 | 1.98 | 4070 | 0.70 | 2.25 |
| vZ 1127 | 4300 | 1.00 | 1.98 | 4225 | 0.90 | 2.00 |
| vZ 1000 | 4200 | 0.65 | 1.94 | 4175 | 0.45 | 2.10 |
| M 13 | | | | | | |
| L 324 | 3990 | 0.10 | 2.34 | 4050 | 0.50 | 2.50 |
| III-56 | 4030 | 0.20 | 2.13 | 4100 | 0.65 | 2.25 |
| L 262 | 4160 | 0.50 | 1.89 | 4180 | 0.80 | 2.00 |

4.2.2. Photometric models

We used recent photometry of our cluster giants, given in Tables 5a and 5b, to derive alternative model atmosphere parameters. The $B - V$ and $V - I$ data were used to derive effective temperatures based on a 12 Gyr isochrone that was constructed with $[\text{Fe}/\text{H}] = -1.54$ and $[\alpha/\text{Fe}] = +0.3$ dex. The luminosities and T_{eff} 's for the models in the isochrone were computed by Dr. D. Vandenberg while Dr. R. Bell performed the luminosity- M_V and the color-temperature transformations. The age of the isochrone (mass) fixes the gravities, while the microturbulent velocities are still determined from spectroscopy. The $V - K$ calibrations are from Cohen, Frogel & Persson (1978). We present the results of the photometric calibrations in Tables 6a and 6b. Using the extrema from the photometric and spectroscopic parameters we derived new model atmospheres from which we determined a range in the abundances allowed by the uncertainties in the models.

4.3. Results

Tables 7a, 7b and 7c present the final results of our abundance analysis for the iron-peak elements, alpha elements and proton-capture elements (those that can be altered in the CNO, NeNa and MgAl nuclear burning cycles), respectively. The numbers in parentheses are the line-to-line scatter for each element while the numbers in the super- and subscripts give the estimated ranges based on variations in the models. We include these latter estimates of uncertainties so that our data can be compared with other observations that use photometric-based atmospheres in the abundance analysis derivations. Clearly, the uncertainty in the abundance determination is dominated more by the uncertainty in the models than by the line-to-line scatter, which we use here as the “error” under the assumption that our models are well-determined.

The Fe-peak elements are consistent with the solar ratio with the exception of nickel, which seems to be under-abundant in all the giants by 0.22 ± 0.03 dex on average. This would be expected if the oscillator strengths for the Ni I lines were overestimated by a similar amount, as indicated in Table 3, which shows our derived oscillator strengths to be 0.20 ± 0.10 dex larger than the literature value. Thus, using the oscillator strengths from the literature would put $[\text{Ni}/\text{H}]$ closer to zero in our sample. Why it should be that the oscillator strengths for Ni would be inconsistent with the published values while those of the other elements are more agreeable remains uncertain. In fact the difference in $\log gf$'s is even larger since our assumed solar Ni abundance is 0.07 dex higher than what Thévenin (1990) assumes; to force agreement with the lower Ni abundance value would cause us to increase our $\log gf$'s by another 0.07 dex.

Figure 5 shows the Fe-peak abundances as a function of T_{eff} for M 3 and M 13. The $[\text{Fe}/\text{H}]$ ratios for M 13 are 0.12 dex lower on average than those for M 3; although, the difference is only at the 1.5σ level. Despite the marginal disparity in $[\text{Fe}/\text{H}]$, the trends for $[\text{V}/\text{Fe}]$, $[\text{Mn}/\text{Fe}]$ and $[\text{Ni}/\text{Fe}]$ are the same for each cluster.

Table 5a. Photometry for M 3 Giants

| Star | Ferraro <i>et al.</i> | | | Rood | | MB | | vB | | SK | | Cudworth | | CFP |
|---------|-----------------------|---------------------|---------------------|---------------------|----------|---------------------|---------------------|----------|---------------------|----------|---------------------|----------|---------------------|---------------------|
| | <i>V</i> | <i>B</i> − <i>V</i> | <i>V</i> − <i>I</i> | <i>V</i> − <i>I</i> | <i>V</i> | <i>B</i> − <i>V</i> | <i>V</i> − <i>I</i> | <i>V</i> | <i>B</i> − <i>V</i> | <i>V</i> | <i>B</i> − <i>V</i> | <i>V</i> | <i>B</i> − <i>V</i> | <i>V</i> − <i>K</i> |
| AA | 12.72 | 1.58 | ... | 1.46 | ... | ... | ... | 12.71 | 1.56 | 12.69 | 1.57 | 3.43 | ... | ... |
| MB 4 | 12.74 | 1.44 | 1.47 | 1.45 | 12.75 | 1.64 | ... | ... | ... | ... | ... | ... | ... | ... |
| III-28 | 12.75 | 1.44 | ... | 1.45 | ... | ... | 1.32 | 12.80 | 1.37 | 12.81 | 1.37 | 3.21 | ... | ... |
| vZ 297 | 12.84 | 1.44 | ... | 1.42 | ... | ... | ... | 12.85 | 1.43 | 12.89 | 1.42 | ... | ... | ... |
| vZ 1127 | 13.09 | 1.29 | 1.47 | 1.35 | ... | ... | ... | ... | ... | 12.93 | 1.23 | ... | ... | ... |
| vZ 1000 | 13.10 | 1.29 | 1.39 | 1.35 | ... | ... | ... | 13.03 | 1.29 | 13.01 | 1.40 | ... | ... | ... |

Table 5b. Photometry for M 13 Giants

| Star | CM79 | | CFP |
|--------|----------|---------------------|---------------------|
| | <i>V</i> | <i>B</i> – <i>V</i> | <i>V</i> – <i>K</i> |
| L 324 | 12.00 | 1.60 | ... |
| III-56 | 12.14 | 1.47 | 3.31 |
| L 262 | 12.25 | 1.39 | ... |

Table 6a. Photometric Models for M 3 Giants

| Star | <i>V</i> – <i>I</i> _{F97} | | <i>B</i> – <i>V</i> _{F97} | | <i>V</i> – <i>I</i> _{FR} | | <i>V</i> – <i>I</i> _{VB} | | <i>V</i> – <i>K</i> _{CFP} | |
|---------|------------------------------------|--------------|------------------------------------|--------------|-----------------------------------|--------------|-----------------------------------|--------------|------------------------------------|--------------|
| | <i>T</i> _{eff} | log <i>g</i> | <i>T</i> _{eff} | log <i>g</i> | <i>T</i> _{eff} | log <i>g</i> | <i>T</i> _{eff} | log <i>g</i> | <i>T</i> _{eff} | log <i>g</i> |
| AA | ... | ... | 3950 | 0.31 | 4061 | 0.57 | ... | ... | 4000 | 0.70 |
| MB 4 | 4060 | 0.57 | 4046 | 0.54 | 4067 | 0.58 | ... | ... | ... | ... |
| III-28 | ... | ... | 4048 | 0.54 | 4070 | 0.59 | 4232 | 0.90 | 4100 | 0.80 |
| vZ 297 | ... | ... | 4043 | 0.54 | 4102 | 0.65 | ... | ... | ... | ... |
| vZ 1127 | 4059 | 0.56 | 4182 | 0.80 | 4189 | 0.81 | ... | ... | ... | ... |
| vZ 1000 | 4088 | 0.62 | 4182 | 0.80 | 4190 | 0.81 | ... | ... | ... | ... |

Table 6b. Photometric Models for M 13 Giants

| Star | <i>T</i> _{eff} | log <i>g</i> |
|--------|-------------------------|--------------|
| L 324 | 3905 | 0.27 |
| III-56 | 4020 | 0.49 |
| L 262 | 4089 | 0.62 |

Table 7a. Fe-Peak Abundances

| Star | [Fe/H] _{FeI} | [Fe/H] _{FeII} | [Fe/H] _{av} | [V/Fe] | [Mn/Fe] | [Ni/Fe] |
|---------|---|---|---|---|---|---|
| M 3 | | | | | | |
| AA | -1.59(0.09) ^{+0.11} _{-0.20} | -1.53(0.08) ^{+0.08} _{-0.11} | -1.57(0.12) ^{+0.12} _{-0.22} | +0.25(0.14) ^{+0.17} _{-0.36} | -0.02(0.16) ^{+0.17} _{-0.26} | -0.22(0.15) ^{+0.15} _{-0.25} |
| MB 4 | -1.55(0.07) ^{+0.07} _{-0.11} | -1.53(0.06) ^{+0.06} _{-0.14} | -1.55(0.09) ^{+0.08} _{-0.12} | +0.19(0.11) ^{+0.14} _{-0.13} | -0.03(0.14) ^{+0.15} _{-0.16} | -0.22(0.14) ^{+0.14} _{-0.20} |
| III-28 | -1.62(0.07) ^{+0.13} _{-0.22} | -1.59(0.07) ^{+0.09} _{-0.09} | -1.61(0.10) ^{+0.12} _{-0.23} | -0.04(0.13) ^{+0.25} _{-0.39} | -0.26(0.11) ^{+0.18} _{-0.24} | -0.28(0.12) ^{+0.16} _{-0.24} |
| vZ 297 | -1.57(0.08) ^{+0.14} _{-0.09} | -1.49(0.07) ^{+0.08} _{-0.07} | -1.55(0.11) ^{+0.14} _{-0.11} | +0.09(0.14) ^{+0.26} _{-0.31} | +0.04(0.16) ^{+0.22} _{-0.17} | -0.25(0.13) ^{+0.15} _{-0.14} |
| vZ 1127 | -1.44(0.09) ^{+0.09} _{-0.40} | -1.50(0.05) ^{+0.05} _{0.15} | -1.45(0.10) ^{+0.10} _{-0.39} | +0.19(0.13) ^{+0.13} _{-0.63} | -0.06(0.13) ^{+0.13} _{-0.41} | -0.25(0.15) ^{+0.15} _{-0.39} |
| vZ 1000 | -1.49(0.10) ^{+0.10} _{-0.24} | -1.50(0.07) ^{+0.07} _{-0.20} | -1.49(0.12) ^{+0.10} _{-0.24} | +0.13(0.15) ^{+0.15} _{-0.37} | -0.14(0.14) ^{+0.14} _{-0.27} | -0.24(0.21) ^{+0.21} _{-0.32} |
| M 13 | | | | | | |
| L 324 | -1.68(0.08) ^{+0.08} _{-0.12} | -1.64(0.07) ^{+0.28} _{-0.07} | -1.67(0.11) ^{+0.31} _{-0.13} | +0.07(0.14) ^{+0.14} _{-0.36} | -0.16(0.11) ^{+0.11} _{-0.22} | -0.24(0.15) ^{+0.17} _{-0.15} |
| III-56 | -1.72(0.07) ^{+0.14} _{-0.08} | -1.64(0.03) ^{+0.05} _{-0.03} | -1.70(0.08) ^{+0.12} _{-0.10} | +0.14(0.11) ^{+0.25} _{-0.15} | -0.09(0.08) ^{+0.16} _{-0.09} | -0.17(0.12) ^{+0.17} _{-0.13} |
| L 262 | -1.61(0.07) ^{+0.07} _{-0.14} | -1.62(0.08) ^{+0.10} _{-0.08} | -1.61(0.11) ^{+0.09} _{-0.14} | +0.15(0.14) ^{+0.14} _{-0.28} | -0.11(0.14) ^{+0.14} _{-0.22} | -0.18(0.14) ^{+0.14} _{-0.20} |

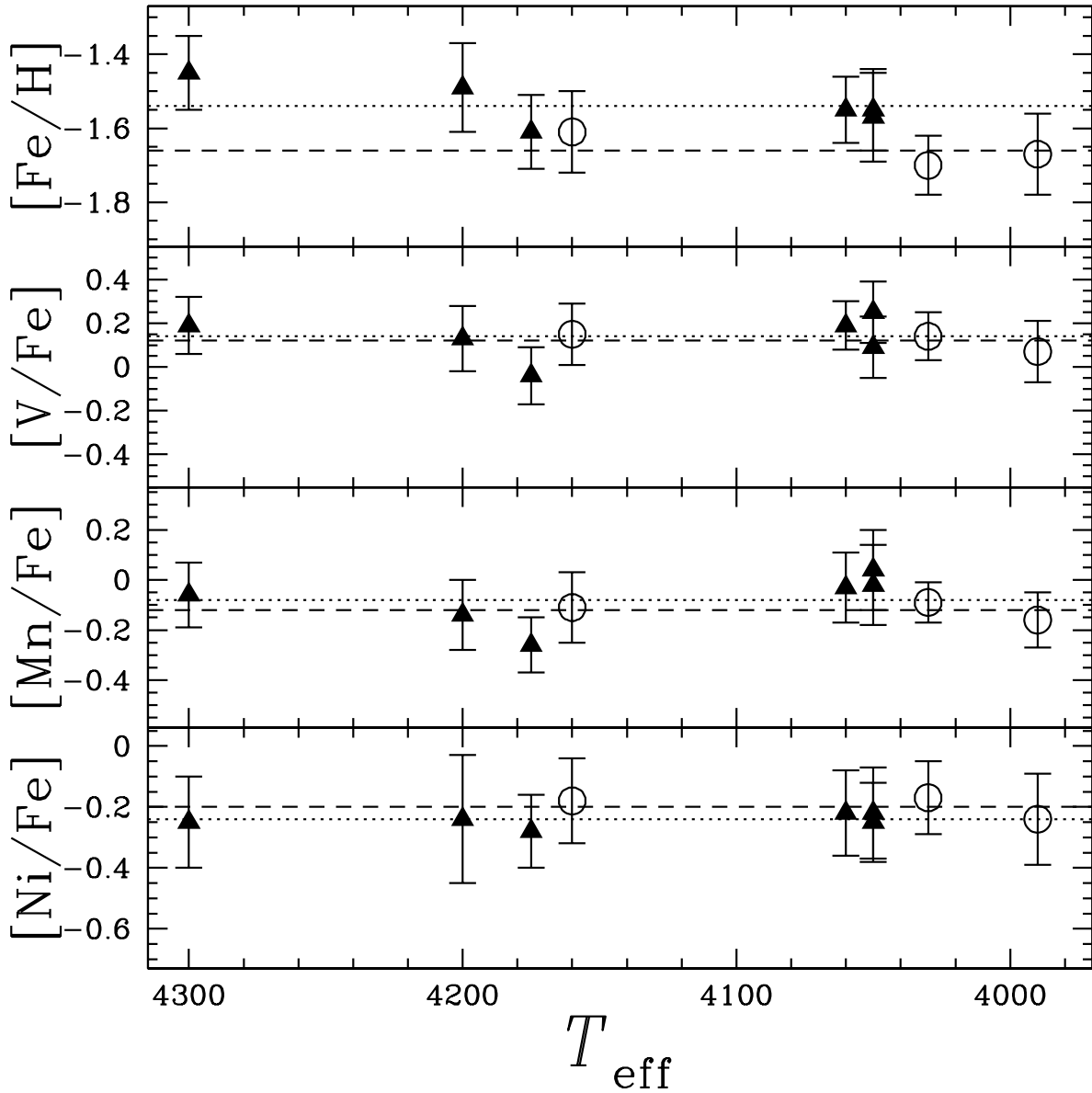


Fig. 5.— Fe-peak abundances as a function of T_{eff} in M 3 (filled triangles) and M 13 (open circles). The dotted and dashed lines are the means for each element for M 3 and M 13, respectively, while the error bars are representative of the line-to-line scatter.

Figure 6 shows the alpha elements as a function of T_{eff} for M 3 and M 13. The alpha element enhancements are consistent with other observations: $[\alpha/\text{Fe}] = +0.28 \pm 0.08$ for M 3 and $+0.30 \pm 0.07$ for M 13. The low dispersions probably indicate that the upper and lower limits from the various model atmospheres overestimate the actual errors in the abundances. The two clusters have very similar alpha enhancements, despite the differences in their iron abundances.

Figure 7 shows the trends in the proton-capture element abundances for all observed stars in M 3 and M 13 as a function of T_{eff} . The oxygen abundances were calculated via the synthetic-spectra fitting package in MOOG and are presented without error bars because 1) they come only from the [O I] line at $\lambda 6300 \text{ \AA}$ so there is no line-to-line scatter, and 2) the spectral resolution around the line is too low to accurately deblend the line from the nearby Sc II line, making attempted variations in the models less meaningful. We estimate the error in $[\text{O}/\text{Fe}]$ to be ~ 0.15 dex. The magnesium abundances are derived from only three lines, all near the edges of the CCD where the noise is high, and are susceptible to large uncertainties. For the M 3 star III-28, we fit a synthetic spectrum to the data around the $\lambda\lambda 6696, 6698$ and $\lambda\lambda 7835, 7836$ Al I regions to determine the abundance and estimate the error to be ± 0.15 dex.

In M 3 $[\text{Al}/\text{Fe}]$ spans a range of 1.1 dex over 250 K and, while the three cooler stars appear to be more enhanced than the three hotter ones on average, it must be cautioned that the sample is biased since the stars were chosen from the Lick/Texas studies based on evidence for or against mixing and is not close to being complete. In addition, the oxygen abundances exhibit a strong anticorrelation with aluminum, but aren't as depleted as in the so-called "super-oxygen-poor" giants in M 13 (Kraft et al. 1992). The sodium abundances likewise show an increasing trend with decreasing T_{eff} and are correlated with $[\text{Al}/\text{Fe}]$. Finally, $[\text{Mg}/\text{Fe}]$ seems fairly independent of T_{eff} and doesn't appear to show any correlations with the other proton-capture elements.

In M 13 it is impossible to make any firm conclusions since the data are so few; however, we note several trends. First, $[\text{O}/\text{Fe}]$ and $[\text{Al}/\text{Fe}]$ are strongly anticorrelated. Second, the aluminum abundance is high (> 0.6 dex) for all three stars, while the oxygen varies from slightly enhanced to fairly depleted (but again, not super oxygen poor). Third, $[\text{Na}/\text{Fe}]$ shows a slight trend of increasing with decreasing T_{eff} . Fourth, the one giant with the strongest aluminum enhancement (L 324) has the strongest magnesium depletion and is also the brightest star in the sample.

5. DISCUSSION

5.1. Evidence for Deep Mixing on the RGB

5.1.1. Theoretical predictions

In Cavallo et al. (1996) and CSB98 we explored the development of the abundance profiles around the H shell of four canonical stellar evolutionary sequences. Although the models were unmixed, we can infer some predictions with regard to deep mixing, which, we remind the reader,

Table 7b. α Abundances

| Star | [Fe/H] _{av} | [Si/Fe] | [Ca/Fe] | [Ti/Fe] _{TiII} | [Ti/Fe] _{TiII} | [Ti/Fe] _{av} |
|---------|----------------------|---|---|---|---|---|
| M 3 | | | | | | |
| AA | −1.57 | +0.42(0.14) ^{+0.14} _{−0.15} | +0.22(0.13) ^{+0.14} _{−0.23} | +0.42(0.15) ^{+0.18} _{−0.34} | +0.40(0.12) ^{+0.12} _{−0.21} | +0.42(0.19) ^{+0.18} _{−0.34} |
| MB 4 | −1.55 | +0.20(0.12) ^{+0.12} _{−0.16} | +0.26(0.12) ^{+0.14} _{−0.13} | +0.45(0.11) ^{+0.13} _{−0.13} | +0.28(0.10) ^{+0.10} _{−0.18} | +0.36(0.15) ^{+0.22} _{−0.26} |
| III-28 | −1.61 | +0.26(0.11) ^{+0.12} _{−0.12} | +0.23(0.14) ^{+0.21} _{−0.28} | +0.25(0.13) ^{+0.25} _{−0.37} | +0.29(0.13) ^{+0.14} _{−0.18} | +0.26(0.18) ^{+0.38} _{−0.24} |
| vZ 297 | −1.55 | +0.37(0.16) ^{+0.16} _{−0.17} | +0.22(0.14) ^{+0.20} _{−0.15} | +0.26(0.15) ^{+0.26} _{−0.16} | +0.21(0.11) ^{+0.13} _{−0.11} | +0.25(0.19) ^{+0.27} _{−0.15} |
| vZ 1127 | −1.45 | +0.17(0.12) ^{+0.12} _{−0.17} | +0.21(0.13) ^{+0.13} _{−0.41} | +0.40(0.11) ^{+0.11} _{−0.57} | +0.35(0.10) ^{+0.10} _{−0.29} | +0.39(0.15) ^{+0.12} _{−0.56} |
| vZ 1000 | −1.49 | +0.29(0.13) ^{+0.13} _{−0.15} | +0.28(0.13) ^{+0.13} _{−0.26} | +0.29(0.14) ^{+0.14} _{−0.35} | +0.20(0.17) ^{+0.17} _{−0.23} | +0.27(0.22) ^{+0.16} _{−0.33} |
| M 13 | | | | | | |
| L 324 | −1.67 | +0.31(0.12) ^{+0.21} _{−0.12} | +0.21(0.13) ^{+0.13} _{−0.28} | +0.34(0.13) ^{+0.13} _{−0.32} | +0.24(0.11) ^{+0.22} _{−0.11} | +0.32(0.17) ^{+0.15} _{−0.30} |
| III-56 | −1.70 | +0.31(0.11) ^{+0.11} _{−0.11} | +0.27(0.12) ^{+0.20} _{−0.12} | +0.28(0.11) ^{+0.26} _{−0.12} | +0.48(0.09) ^{+0.16} _{−0.09} | +0.32(0.14) ^{+0.32} _{−0.16} |
| L 262 | −1.61 | +0.45(0.13) ^{+0.14} _{−0.13} | +0.22(0.14) ^{+0.14} _{−0.21} | +0.29(0.12) ^{+0.12} _{−0.25} | +0.40(0.11) ^{+0.11} _{−0.14} | +0.31(0.16) ^{+0.20} _{−0.27} |

Table 7c. Proton-Capture Abundances

| Star | [Fe/H] _{av} | [O/Fe] | [Na/Fe] | [Mg/Fe] | [Al/Fe] |
|---------|----------------------|--------|---|---|---|
| M 3 | | | | | |
| AA | −1.57 | −0.03 | +0.42(0.13) ^{+0.14} _{−0.19} | +0.25(0.12) ^{+0.13} _{−0.14} | +0.87(0.14) ^{+0.14} _{−0.20} |
| MB 4 | −1.55 | −0.05 | +0.42(0.10) ^{+0.13} _{−0.10} | +0.18(0.13) ^{+0.13} _{−0.14} | +0.83(0.13) ^{+0.14} _{−0.13} |
| III-28 | −1.61 | +0.36 | ... | −0.01(0.11) ^{+0.13} _{−0.18} | −0.19(0.15) |
| vZ 297 | −1.55 | −0.01 | +0.13(0.15) ^{+0.19} _{−0.16} | +0.05(0.11) ^{+0.14} _{−0.11} | +0.71(0.13) ^{+0.17} _{−0.13} |
| vZ 1127 | −1.45 | +0.33 | −0.22(0.10) ^{+0.10} _{−0.28} | +0.01(0.13) ^{+0.13} _{−0.25} | −0.01(0.11) ^{+0.11} _{−0.28} |
| vZ 1000 | −1.49 | −0.01 | +0.17(0.12) ^{+0.13} _{−0.20} | +0.18(0.13) ^{+0.13} _{−0.19} | +0.72(0.14) ^{+0.14} _{−0.21} |
| M 13 | | | | | |
| L 324 | −1.67 | −0.38 | +0.54(0.12) ^{+0.12} _{−0.23} | −0.02(0.13) ^{+0.13} _{−0.15} | +0.99(0.12) ^{+0.12} _{−0.19} |
| III-56 | −1.70 | −0.05 | +0.50(0.08) ^{+0.13} _{−0.09} | +0.23(0.16) ^{+0.19} _{−0.17} | +0.74(0.11) ^{+0.16} _{−0.11} |
| L 262 | −1.61 | +0.11 | +0.34(0.11) ^{+0.11} _{−0.16} | +0.10(0.14) ^{+0.14} _{−0.17} | +0.61(0.13) ^{+0.13} _{−0.17} |

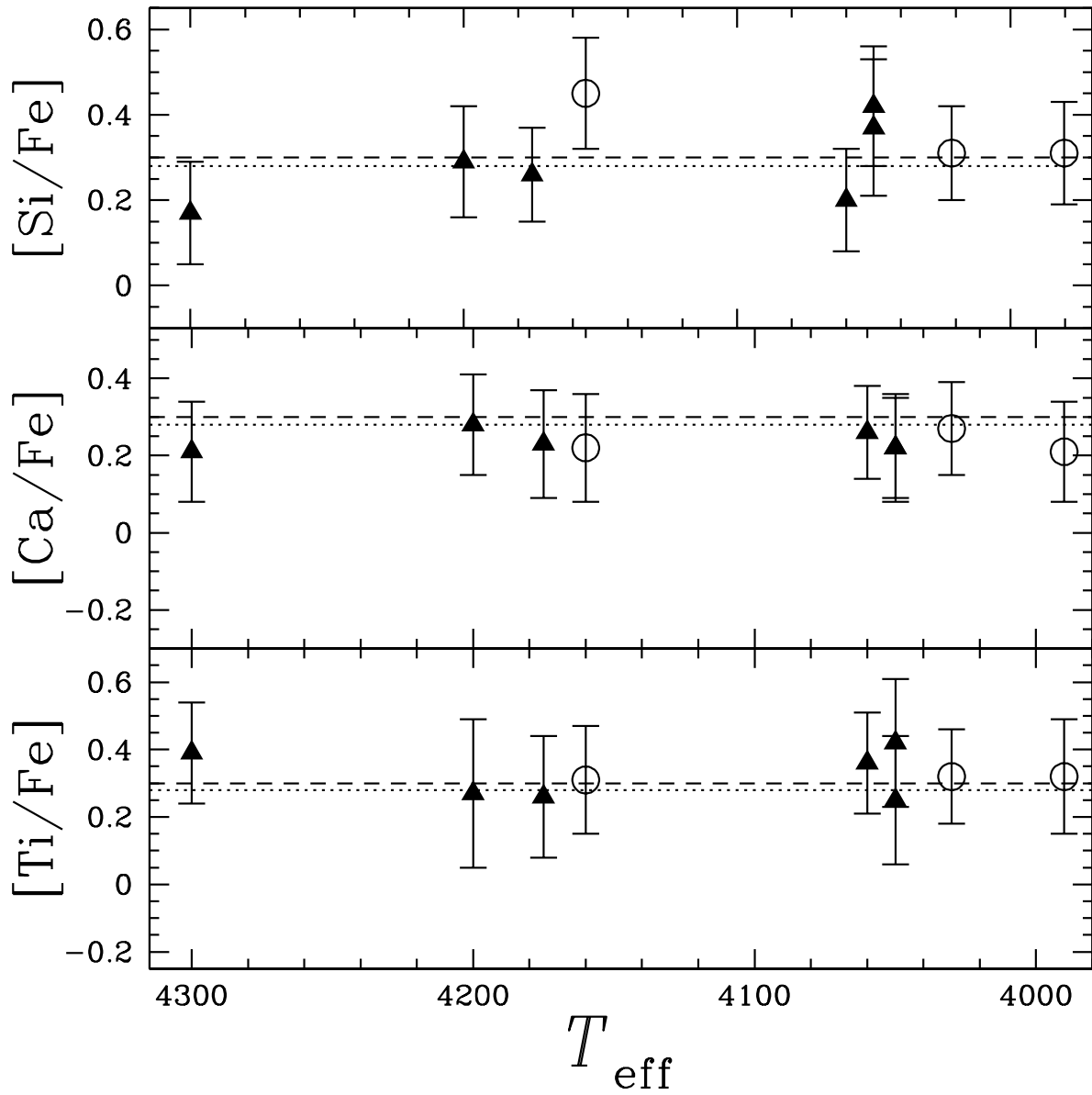


Fig. 6.— The alpha elements as a function of T_{eff} in M 3 (filled triangles) and M 13 (open circles). The dotted and dashed lines are the means for each element for M 3 and M 13, respectively, while the error bars are representative of the line-to-line scatter.

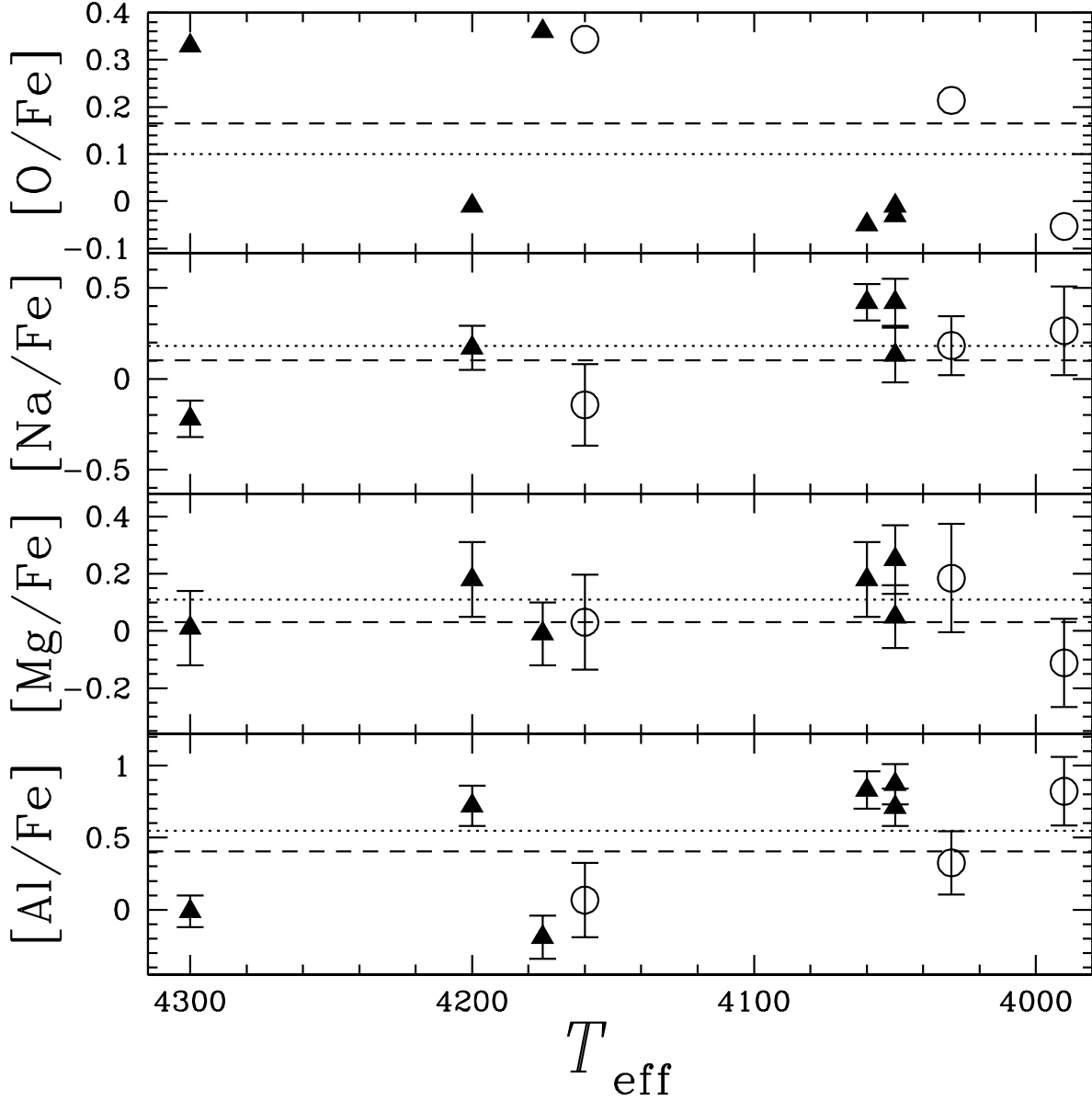


Fig. 7.— The proton-capture elements as a function of T_{eff} in M 3 (filled triangles) and M 13 (open circles). The dotted and dashed lines are the means for each element for M 3 and M 13, respectively, while the error bars are representative of the line-to-line scatter.

is defined as mixing that penetrates the H shell.

- Carbon, nitrogen and oxygen are not good tracers of deep mixing since they are easily altered above the H shell in the CN and ON nuclear reaction cycles.
- Sodium is altered above the H shell from ^{22}Ne and inside the H shell from ^{20}Ne through the NeNa cycle as shown in Figure 8. The proton-capture rates for the NeNa cycle are still uncertain and the initial neon abundance in real RGB stars is impossible to measure, making the theoretical prediction of actual sodium enhancements difficult.
- As shown in Figure 8, ^{27}Al , the only stable aluminum isotope, is enhanced only inside the H shell at the expense of mostly ^{25}Mg plus ^{26}Mg , but also some ^{24}Mg deep inside the H shell for very bright, metal-poor models. The reaction rates for the MgAl cycle are still subject to large uncertainties; although, the ^{24}Mg proton capture rates are now well-determined (Powell et al. 1999).
- Aluminum enhancements are temperature sensitive, indicating that they should not be expected until higher luminosities are achieved in lower metallicity giants ($[\text{Fe}/\text{H}] \lesssim -1.2$). In addition, the creation of sodium from ^{20}Ne also requires the high temperatures found only inside the H shell of the same bright, metal-poor giants, indicating that large sodium enhancements that originate with this neon isotope occur only towards the RGB tip.

All these inferences are still subject to uncertainties in the source of mixing, the initial abundances and the nuclear reaction rates; nonetheless, we now venture to compare the observational data with the theoretical predictions.

5.1.2. *Observational results: the aluminum data*

In addition to the M 13 aluminum abundances determined above, we were provided with the equivalent-width data of the Al I $\lambda 6696$ Å line for 78 more giants in this cluster that were obtained from spectra taken with the WIYN telescope and Hydra multi-object spectrograph by Dr. C. Pilachowski in an attempt to find spurious Li I features at $\lambda 6707$ Å (Pilachowski et al. 2000), as found in the M 3 giant IV-101 by Kraft et al. (1999)¹⁰. The details of the data reduction and search results for her study will be reported on elsewhere (Pilachowski et al. 2000). Since the Li I line is so strong, the exposures were short in order to probe as many stars as possible. Unfortunately, this resulted in a lower signal-to-noise ratio than preferred for the nearby Al I lines, but the data are reliable for stars with strong aluminum lines: of the 78 giants in the WIYN dataset, 66 had measurable equivalent widths. To derive the aluminum abundances, the equivalent widths were folded through models that were built using the MARCS code based on the atmospheric

¹⁰We find no evidence of this feature in any of our M 3 or M 13 spectra.

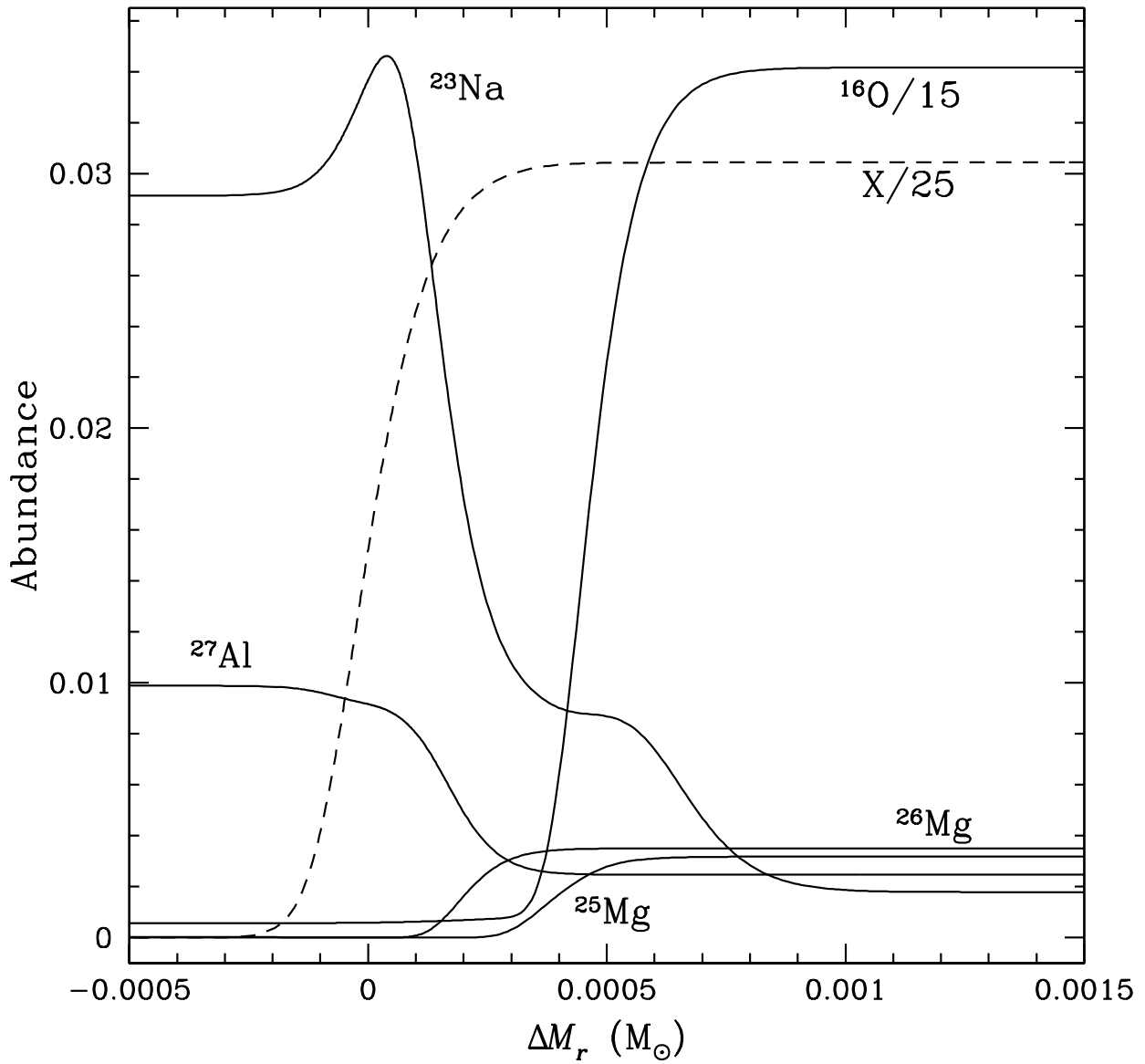


Fig. 8.— The abundance variations around the H shell of a red-giant-branch tip model with $[\text{Fe}/\text{H}] = -1.67$ and scaled solar composition. The abscissa is the mass difference between any point and the center of the H shell. Hydrogen and helium are given in mass fractions while the other elements are scaled relative to the total number of metals.

parameters that were initially derived via photometry (Pilachowski et al. 1996). The models were assumed to have $[\text{Fe}/\text{H}] = -1.50$, while, as with the models from this present study, the $[\alpha/\text{Fe}]$ ratio was also assumed to be enhanced by +0.4 dex. As shown in Tables 5, 6 and 7, models based on photometric indices can lead to a wider range of abundances; although, we believe the WIYN models to be well-determined since they were iteratively corrected with the spectra.

Of the twelve other stars in the WIYN sample that did not have measurable lines, one, II-76, had an aluminum abundance previously determined in the literature; $[\text{Al}/\text{Fe}] = -0.19$ (Shetrone 1996a). The other eleven were assumed to have $[\text{Al}/\text{Fe}] = 0$ for the purposes of the statistics discussed below, an assumption that seems verified by II-76 having such a low aluminum abundance; although, this star is rather bright while the other eleven are much lower magnitude examples. The three M 13 stars observed by us were also present in the WIYN sample and the abundances agreed to within the errors from the line-to-line scatter. Although the differences between the 4-m data and the WIYN data are small, systematic errors can arise since the WIYN models are rooted in photometry with corrections to T_{eff} and v_t from lower resolution spectra (see Pilachowski et al. 1996 for details). For example, our models are 40-60 K hotter, have gravities that are 0.35-0.45 dex lower and microturbulent velocities that are 0.09-0.13 km s^{-1} higher. In addition, our spectra have a factor of two higher resolution than the WIYN data and our signal-to-noise ratios are significantly higher.

Finally, the sample was then augmented with $[\text{Al}/\text{Fe}]$ values taken from the literature (Wallerstein et al. 1987; Shetrone 1996a; Kraft et al. 1997), bringing the total number of stars with determined $[\text{Al}/\text{Fe}]$ values to 85. We believe that the systematic errors that might be present in the data are mostly removed before combination since, with the exception of Wallerstein et al. (1987) for two stars, they are derived by the same group of Lick/Texas observers who practice consistent reduction techniques. Small differences will arise as the telescopes and instruments are varied, but the Lick/Texas observers do compare their various observations and show little scatter among their results. If one adds the eleven stars with the assumed low $[\text{Al}/\text{Fe}]$ values, the total sample size is 96, covering a range from the tip of the RGB at $V = 11.9$ to $V = 15.5$, with complete coverage of the Cudworth & Monet (1979) photometry for $V \lesssim 13.7$. The data are plotted in Figure 9a as a function of V magnitude, where the eleven stars with $[\text{Al}/\text{Fe}]$ assumed to be 0 are shown as open circles. The $[\text{Al}/\text{Fe}]$ values of giants with multiple measurements were averaged together after being normalized by $[\text{Fe}/\text{H}]$.

In Figure 9c we show a histogram of the distribution of $[\text{Al}/\text{Fe}]$ for the entire sample of 96 M 13 giants. From this figure, we see an apparent gap between $[\text{Al}/\text{Fe}] = 0.2$ and 0.4, indicating that the distribution might be bimodal. We test for bimodality by applying the KMM algorithm of Ashman et al. (1994), which tests the null hypothesis that a single Gaussian is a good description of the data by comparing the fit of a single-peaked distribution to one with multiple modes. The algorithm returns a P -value that describes the confidence level of the single-mode fit, where $P < 0.05$ indicates that a single Gaussian can be rejected at better than the 95% confidence level, which is generally accepted as strongly consistent with the multimodal distribution. Testing for a bimodal

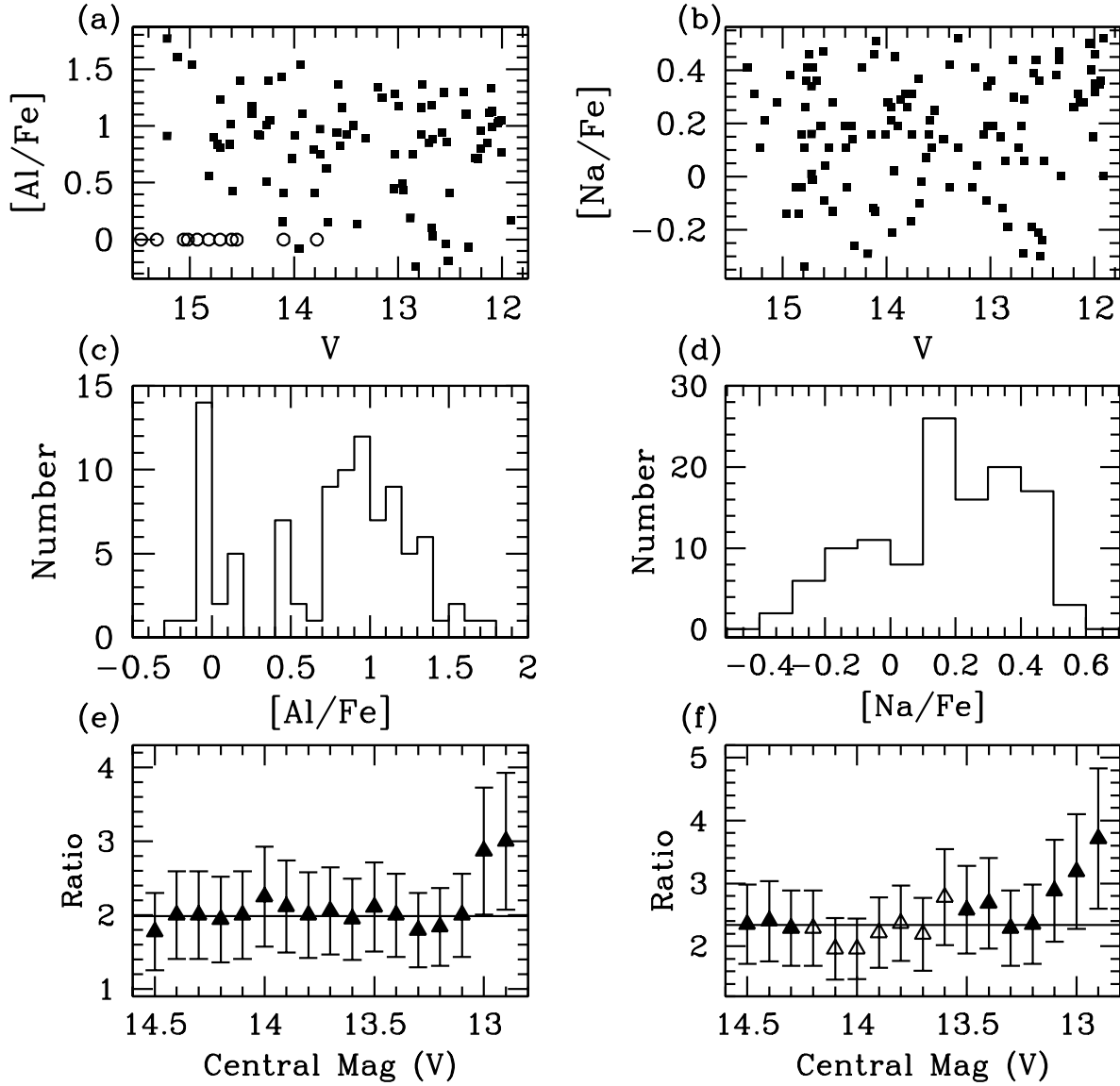


Fig. 9.— (a) $[\text{Al}/\text{Fe}]$ values of M 13 giants as a function of V magnitude. Measured values are shown as filled squares, while those with assumed values are shown as open circles. In the cases where multiple measurements for the same star exist, the values are averaged together after being normalized by $[\text{Fe}/\text{H}]$. (b) Same as (a), except for $[\text{Na}/\text{Fe}]$. (c) A histogram of the $[\text{Al}/\text{Fe}]$ distribution in M 13. (d) Same as (c) except for $[\text{Na}/\text{Fe}]$. (e) The Al ratio in M 13 as a function of magnitude as determined by the KMM algorithm. The thick solid line is the mean of the 15 points at $V > 13.0$. (f) The Na ratio in M 13 as a function of magnitude as determined by the KMM algorithm. The open triangles indicate where the distribution is likely unimodal. The thick solid line is the mean of the 14 points at $V > 13.1$.

distribution in our sample gives $P = 0.000$ with means in [Al/Fe] of 0.12 ± 0.25 for the “Al-normal” peak and 1.03 ± 0.25 for the “Al-enhanced” peak. The number of stars in each distribution is 65 and 31 for the Al-enhanced and Al-normal groups, respectively, giving a ratio of Al-enhanced to Al-normal stars (hereafter, the “Al ratio”) of 2.10 ± 0.46 , where the error is estimated from Poissonian statistics.

It is possible that our assumption concerning the actual [Al/Fe] values of stars with no measurable Al I lines can introduce a bias into our statistics. For example, Pilachowski et al. (2000) report an upper limit of $20 \text{ m}\text{\AA}$ for equivalent width measurements of lower luminosity giants. Applying this measurement to the star K 272, which has $V = 15.47$, and using the model parameters supplied by Pilachowski et al. (2000), we obtain $[\text{Al/Fe}] \leq 0.88$, assuming $[\text{Fe/H}] = -1.49$. We test the effect of this bias by subjecting just the 85 giants with actual aluminum measurements to the KMM algorithm, yielding a P -value of 0.002, with an Al-ratio of 3.72 ± 0.98 . This clearly demonstrates that removal of the uncertain data still results in a strongly bimodal distribution. The only real solution to correct this possible bias is to make higher signal-to-noise observations.

If deep mixing is occurring on the RGB, then the Al ratio should be a function of magnitude, increasing with decreasing V . To test this hypothesis we bin the data by magnitude and apply the KMM algorithm to each bin to determine whether the distribution in each bin is bimodal and, if it is, the Al ratio. The KMM algorithm requires that the number of data points be greater than 50, forcing the size of magnitude bins to be rather wide ($\Delta V = 2$) in order to ensure that enough stars are included for reliable statistics. We began our binning at $V = 12.9$, one magnitude lower than the brightest star in the sample, and shift each bin by 0.1 magnitude up to $V = 14.5$, one magnitude brighter than the lowest luminosity star in the sample. This choice of bins avoids adding empty points along the RGB into our statistics; although, it reaches magnitudes where the sample is incomplete. According to the KMM algorithm, the aluminum distribution in each magnitude bin is bimodal, with all P values less than 0.013 and most less than 0.004. In Figure 9e we show the Al ratio (with Poissonian error bars) as a function of the central magnitude of each bin. The mean of the 15 points between $V = 13.1$ and 14.5 is 1.99, which is shown as the solid horizontal line in Figure 9e. The Al ratios in the second brightest and brightest magnitude bins are 2.9 and 3. The upturn at the brighter magnitudes is due to both an increase in the number of Al-enhanced stars and a decrease in the number of Al-normal stars, as can be seen in Figure 9a, and is consistent with mixing occurring along the RGB; although, the error bars do not allow for a definitive conclusion in this regard.

We now compare the M 13 data with those from M 3, where the number of giants with measured Al abundances is substantially smaller. Although we augment our sample of six giants in M 3 with an additional four that were observed by Kraft et al. (1999, none in common with our sample), the numbers are still too small to apply the KMM algorithm; however, as shown in Figure 10a, the M 3 [Al/Fe] distribution appears bimodal, with an Al ratio of 1.5 ± 1.0 . This is consistent with the presumably unmixed dimmer giants in M 13, suggesting that deep mixing is not occurring in M 3.

5.1.3. Observational results: the sodium data

We incorporated the [Na/Fe] data from our three M 13 giants with the literature values (Lehnert et al. 1991; Kraft et al. 1992, 1993, 1995; Pilachowski et al. 1996; Shetrone 1996a,b; Kraft et al. 1997) to build a database containing 119 M 13 RGB stars with measured sodium abundances, which we show in Figure 9b as a function of V . Again, we believe the systematic errors associated with the combination of various data sets to be minimized for the reasons outlined in the previous section. As demonstrated in Figures 9a and 9b, and in Figure 11 for a subset of stars that have both [Al/Fe] and [Na/Fe] values determined, the range in [Na/Fe] is not as wide as in the [Al/Fe] data, with the [Na/Fe] values being both more negative for “low” sodium stars and not as enhanced for the “high” sodium stars. However, from Figure 9b it is clear that the tip of the RGB does lack sodium-poor giants, if [Na/Fe] = 0 can be considered a high value relative to the rest of the low-Na distribution.

A histogram of the total sodium distribution is shown in Figure 9d, where two peaks are apparent, but with no obvious gap between them. However, application of the KMM algorithm does indicate a bimodal distribution ($P = 0.001$) with two peaks at [Na/Fe] = -0.09 ± 0.13 and $+0.29 \pm 0.13$. The low sodium group has 33 members, while the high sodium group has 86, for a ratio of Na-enhanced to Na-poor giants (hereafter, the “Na ratio”) of 2.61 ± 0.53 . Since the peaks are not widely separated (2.93σ), it is difficult to determine to which group stars between the peaks belong, making the above ratio less certain. The KMM algorithm provides two group membership probabilities (GMPs) for each star, which give the percentage probability that a value belongs to “high” and “low” mode (the sum of the GMPs for each star equals 100%). For the sample of M 13 giants, 35 stars (30%) have both GMPs between 10% and 90%, indicating that these stars cannot be assigned to either mode with high confidence.

When we bin the [Na/Fe] values by magnitude, as with the [Al/Fe] data, the bimodality of the distribution within each bin is not as certain as with the entire sample. We demonstrate this in Figure 9f, where we show the Na ratio for M 13 in two-magnitude wide bins. The open triangles in this figure represent ratios where the P -values are greater than 0.05, indicating that a unimodal Gaussian is not easily ruled out as the “true” parent distribution. The filled-in triangles at $V > 14.2$ represent apparently bimodal distributions; however, the stars at these lower magnitudes are undersampled, confounding efforts to determine the nature of the [Na/Fe] distribution in M 13.

Despite the uncertainty at lower magnitudes, the [Na/Fe] distribution for the brighter M 13 giants is likely bimodal according the KMM statistics and is similar to that of the [Al/Fe] distribution. The mean of the 14 dimmest points is 2.33, represented by the solid line in Figure 9f. Relative to the mean, the upturn at $V = 13.1$ appears real and is due to the lack of low-sodium stars $V \lesssim 12.5$, as seen in Figure 9b.

We compare the distribution of sodium in M 3 with that of M 13. As with the aluminum data, the sample size is small, with only fourteen M 3 stars having determined [Na/Fe] values (Kraft et al. 1992, 1993, 1995, 1999), six of which are also determined above. We believe the systematic

differences among the Lick/Texas results and between our data and theirs that arise from the use of different telescopes, instruments and reduction techniques are not significant enough to affect the interpretation of the results. As can be seen in Figure 10b the distribution is fairly flat with eight stars having $[\text{Na}/\text{Fe}] \leq 0.00$ and only three with $[\text{Na}/\text{Fe}] > +0.3$. This is more consistent with limited mixing, but the numbers are much too small to draw realistic conclusions.

5.1.4. *Observational results: sodium and aluminum*

Referring again to Figure 11, we look for a correlation between sodium and aluminum in M 13 by comparing the 62 giants with measured values of both $[\text{Al}/\text{Fe}]$ and $[\text{Na}/\text{Fe}]$. The data appear correlated, with a linear correlation coefficient of 0.723, which according the probability coefficient given in Appendix C of Taylor (1982), is “highly significant” for this sample size. We do note, however, that at $[\text{Al}/\text{Fe}] \sim +0.5$, the full range of $[\text{Na}/\text{Fe}]$ values is present, making the correlation suspicious around this narrow range of $[\text{Al}/\text{Fe}]$ values.

Applying the KMM algorithm to just these 62 stars reveals that both the aluminum and sodium distributions are bimodal, with each having $P = 0.000$, and an Al ratio and a Na ratio both equal to 3.13 ± 0.93 . To test whether the identical ratios are just coincidence or if indeed, a star with high $[\text{Al}/\text{Fe}]$ is likely to have high $[\text{Na}/\text{Fe}]$ and vice-versa, we examine the difference in the GMPs between the aluminum and sodium data for the “high” modes, as shown in the histogram in Figure 12.

If the abundances of aluminum and sodium are correlated then the difference between the GMPs will be close to zero, as seems to be the case for most giants since 52 stars fall between -0.10 and $+0.10$. However, ten deviate from zero by more than 0.25; so that while Figure 12 indicates that only two or three giants do not fit into the correlation around $[\text{Al}/\text{Fe}] = +0.5$, the KMM algorithm actually shows that this number is larger and that around 16% of the sample are not statistically correlated. We must also reiterate that the $[\text{Al}/\text{Fe}]$ values from the WIYN sample are not always well-determined and these numbers are likely to change with better data. In general, the correlation between $[\text{Al}/\text{Fe}]$ and $[\text{Na}/\text{Fe}]$ seems fairly constrained; however, we suggest that when testing for deep mixing, aluminum is a better element to observe than sodium since the data show that the distinction between high and low $[\text{Al}/\text{Fe}]$ is clearer and the models suggest that aluminum is produced much closer to the H shell than sodium. According to the models, the appearance of *mixing-enhanced* aluminum on the surface of a star should imply the existence of extra sodium, while the converse is not necessarily true. The fact that the data show that 84% of the time the abundance of one element is a predictor of the other indicates just how deeply mixed the M 13 giants probably are.

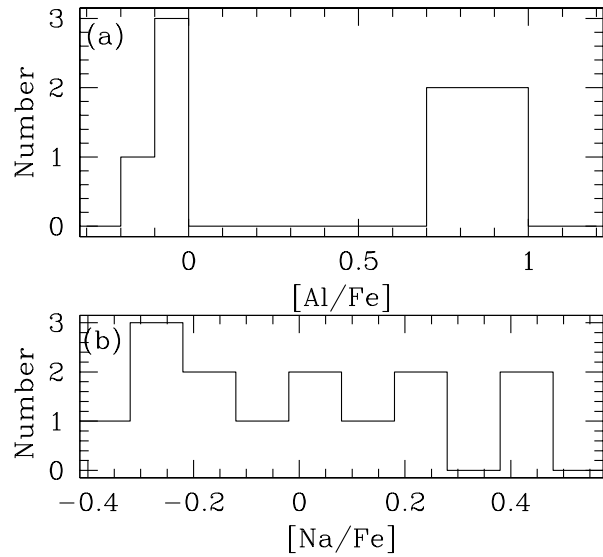


Fig. 10.— A histogram of (a) the $[\text{Al}/\text{Fe}]$ and (b) the $[\text{Na}/\text{Fe}]$ distributions in M 3.

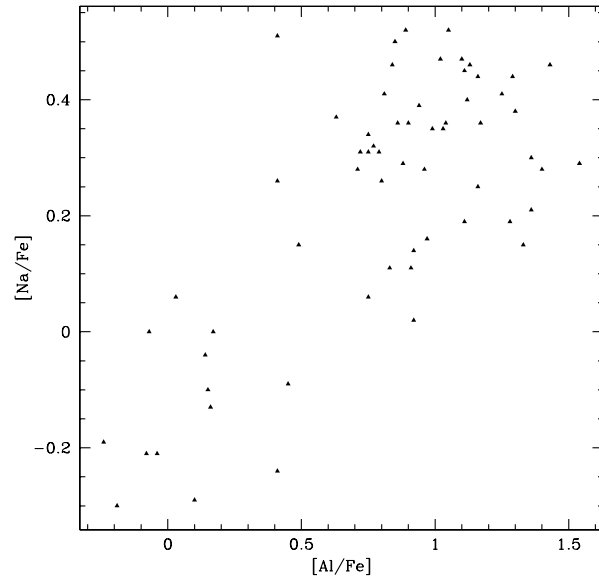


Fig. 11.— $[\text{Na}/\text{Fe}]$ versus $[\text{Al}/\text{Fe}]$ for 62 giants in M 13.

5.2. Hot Flashes and Primordial Influences

Enhanced aluminum abundances at magnitudes much lower than the tip of RGB are difficult to explain with mixing models since the peak temperature of the H shell is not high enough to produce a significant amount of aluminum at this stage of evolution (Cavallo et al. 1998). What then is the source of the high aluminum abundances at these lower luminosities? Some have suggested that the H shell might become unstable at lower magnitudes due to rotation and can undergo flashes that result in peak temperatures near 70 MK or higher (Langer et al. 1997; Fujimoto et al. 1999), as opposed to the canonical temperatures below 60 MK (see, e.g., CSB98). This hot temperature was chosen specifically by Langer et al. (1997) because it reproduces the observed abundance anomalies in some M 13 giants, particularly the ^{24}Mg depletions and aluminum enhancements observed by Shetrone (1996b). Unfortunately, such an exercise depends strongly on the accuracy of the nuclear reaction rates, which, in many cases, are not very well determined [see, e.g., the NACRE (Angulo et al. 1999) compilation¹¹]. Also, in addition to the fact that the H-shell instabilities have yet to be demonstrated in RGB models, it is not clear what the effects of such flashes would be on the structure and evolution of a star. For example, would these flashes have observable consequences that affect the RGB luminosity function, which is generally well-reproduced by canonical evolutionary models? Furthermore, the instability scenario of Langer et al. (1997) only applies to the lower RGB (Von Rudloff et al. 1988), which is at odds with the data reported here that show aluminum and sodium enhancements occur towards the tip of the RGB; if these elements were being produced on the lower RGB via hot flashes, the Al and Na ratios would vary at lower magnitudes. In the case of the Fujimoto et al. (1999) scenario, which involves continually peeling off layers of the core and completely disrupting the H shell, it is not clear how stars can evolve up the RGB and not have serious consequences for the observed luminosity functions of clusters in which the RGB members experience deep mixing.

We suggest that a more favorable location for hot hydrogen burning is around the H shell of intermediate-mass ($M > 4M_{\odot}$) AGB stars (referred to as IMS), which undergo hot bottom burning (HBB), so called because the convective envelope is in contact with the H shell. The IMS could have shed their nuclearly processed envelopes that include enhanced aluminum and sodium abundances into the early cluster environment (Cottrell & Da Costa 1981; Denissenkov et al. 1997, 1998), creating the observed abundance distributions. For example, the bimodality of [Al/Fe] values on the lower RGB would be created if the ejecta were distributed locally. Likewise, the [Na/Fe] distribution in both clusters is explained if the IMS envelopes were also enriched in sodium. Unfortunately, detailed and accurate aluminum and sodium abundance yields from metal-poor AGB evolution models are non-existent; but the high temperatures of HBB in IMS, and the observations themselves, lend some weight to this hypothesis.

¹¹ Also available at <http://pntpmlab.ac.be/nacre.htm>

5.3. Results from a Deep Mixing Algorithm

We have taken the models described in CSB98 and subjected them to a deep mixing algorithm that assumes that the mixing is instantaneous; i.e., the mixing timescale is the same as the nuclear burning timescale. A complete derivation of our algorithm is given in the appendix. While this simplified approach is unable to mimic a realistic mixing timescale, it does have several advantages: 1) it can give an upper limit to the amount of variation an element can experience due to nuclear processing, 2) it can show the lowest point on the RGB where an element can be processed and 3) it can be used to check the effect of the uncertainties in the nuclear reaction rates on the envelope abundances (Cavallo 1998b). We discuss the first two points after a brief description of the algorithm.

The nuclear reaction network employed in the mixing algorithm is the same as the one used in CSB98 with the following modifications. We use updated rates for the $^{26}\text{Mg}(p, \gamma)^{27}\text{Al}$ reaction that have been provided to us by C. Rowland. Her rates are 1) approximately 10 - 16 times faster than the NACRE rates (Angulo et al. 1999), 2) 1.5 to 4.5 times faster than the rates used in CSB98 and 3) commensurate with the Caughlin & Fowler (1988) tables in the range of $T_9 = 0.4 - 0.6$, where $T_9 = 10^9$ K. The ^{26}Al proton-capture rate has been separated into the short-lived isomeric state, ^{26m}Al , and the meta-stable ground state, ^{26g}Al (this had a negligible impact on the conclusions drawn in CSB98). The NACRE compilation shows that the ^{26g}Al proton-capture rate is uncertain by three orders of magnitude, the effects of which are discussed in the conclusions. We use the rates for the $^{24}\text{Mg}(p, \gamma)^{25}\text{Al}$ reaction that have been updated by Powell et al. (1999), who measured the resonance parameters of the $E_R = 223$ keV resonance to show that the low-energy contribution to the total rate does not significantly increase this rate as suggested by Zaidins & Langer (1997). The new rates show a 32% increase over the commonly used Caughlin & Fowler (1988) rates in the range of $T_9 = 0.4 - 0.6$, which is not enough to account for the observed depletions of ^{24}Mg in a handful of M 13 and NGC 6752 giants observed by Shetrone (1996b, 1997).

The initial abundances that we put into our algorithm are those of Denissenkov et al. (1998), who suggest using $[\text{Mg}/\text{Fe}] = +1.1$ dex as the result of AGB contamination, while the initial $[\text{Mg}/\text{Fe}]$ and $[\text{Mg}/\text{Fe}]$ both equal 0. This suggestion is further backed by recent results of Lattanzio et al. (1999) who find the overproduction of ^{25}Mg and ^{26}Mg relative to ^{24}Mg in metal-poor AGB models. In addition, we enhance the other α elements by +0.4 dex.

We assume mixing begins on the part of the RGB where the H shell burns through the hydrogen discontinuity left behind after the first dredge-up, in accordance with the assumption that large μ barriers can prevent mixing at earlier epochs (SM79). This point along the RGB corresponds to the well-known “bump” in the luminosity function (Fusi Pecci et al. 1990). Supporting this choice are the theoretical mixing models by Charbonnel (1994, 1995) that also assumed mixing begins at this point and reproduced the observed variations of the $^{12}\text{C}/^{13}\text{C}$ ratio, ^7Li and the $^{12}\text{C}/^{14}\text{N}$ ratio in both open and globular clusters. In addition, the observations of Bell et al. (1979), Suntzeff (1981), Gilroy & Brown (1991), Grundahl (1999) and Carretta et al. (1999) also support this choice for the

onset of mixing. We do point out that not all observations support this choice as the onset mixing (Carbon 1982; Trefzger et al. 1983; Langer et al. 1986; Briley et al. 1990), however, the exact start of deep mixing will little affect our final results.

The timestep for nuclear processing fixes the timestep for mixing and is controlled by setting a limit on how fast any element above a minimum abundance threshold may vary. Since this timestep is much shorter than the time difference between the models used in CSB98, new models were interpolated along the RGB until the He flash was encountered. The free parameters in our code are ΔX , the mixing depth defined by a change in the H-mass fraction, X , within the H shell, and η , Reimers' mass-loss parameter (Reimers 1975). The algorithm was run with various combinations of mixing depths and mass-loss rates for a stellar evolution sequence having $[\text{Fe}/\text{H}] = -1.67$.

Figure 13 shows the $[\text{Al}/\text{Fe}]$ values derived from our algorithm as a function of absolute magnitude, parameterized by various mixing depths and mass-loss rates. The absolute magnitude scale was derived from the bolometric luminosity, L , and T_{eff} provided by the models. We first converted $\log(L/L_{\odot})$ into the bolometric magnitude, M_{bol} , using the sun as a reference with a value of 4.75 for $M_{bol\odot}$. Next, we used the following relationship between gravity, g , mass, M , T_{eff} and L to obtain $\log g$ for each model:

$$\log g = \log(M/M_{\odot}) + 4\log T_{\text{eff}} - \log(L/L_{\odot}) - 10.61028, \quad (1)$$

where a value of $T_{\text{eff}\odot} = 5780$ K is assumed. Mass loss is implicitly accounted for via the first term on the right hand side of equation 1. Using a 12 Gyr isochrone with $[\text{Fe}/\text{H}] = -1.67$, also constructed by Drs. Vandenberg and Bell, we interpolated according to $\log g$ to find a bolometric correction then converted M_{bol} into M_V . We show the results for $\Delta X = 0.05, 0.10, 0.15$ and 0.20 , and for $\eta = 0.0, 0.2, 0.4$ and 0.6 at each ΔX , as described in the figure caption.

According to Figure 13, the dominant parameter for determining $[\text{Al}/\text{Fe}]$ at the RGB tip is the mixing depth. Mass loss plays a secondary role for deeply mixed models but is more important for less deeply mixed models. The importance of η is controlled by a competition between the timescale for mass loss and the timescale for converting magnesium into aluminum: for a given sequence, the mass-loss timescale is fixed by η , so that with deeper mixing, the Mg-burning timescale decreases, bringing the two closer together and limiting the influence of mass loss. Thus, in the limit of instantaneous mixing, the distribution of $[\text{Al}/\text{Fe}]$ near the tip of the RGB is due primarily to variations in the mixing depth; although, for the deeply mixed sequences, the value of $[\text{Al}/\text{Fe}]$ at the tip begins to saturate.

One factor that depends strongly on the mixing depth is the earliest point along the RGB where mixing-induced aluminum variations can occur. In Figure 13 we draw a dashed vertical line at $[\text{Al}/\text{Fe}] = +0.4$ to indicate where the aluminum enhancements cross the into the “high” aluminum distribution for M 13 giants. Our results show that for the mixing depths shown in Figure 13, large aluminum enhancements should appear along the brightest ~ 1.5 to 0.5 magnitudes of the RGB. A change in ΔX from 0.05 to 0.20 results in a one magnitude difference in where the aluminum abundance rises on the RGB. We apply these estimates to the M 13 sample by binning the data

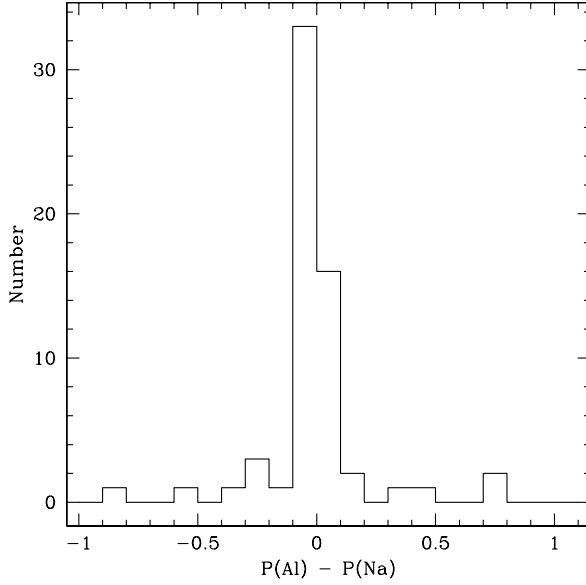


Fig. 12.— A histogram of the differences between the group membership probabilities for aluminum and sodium for the stars in Figure 11.

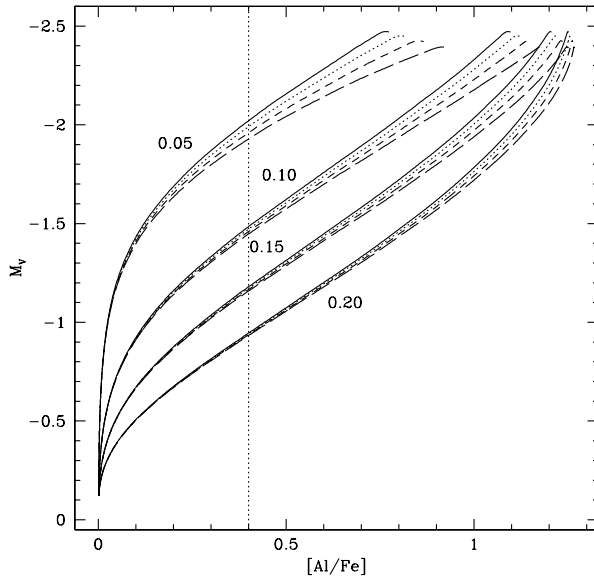


Fig. 13.— The predicted variation in $[\text{Al}/\text{Fe}]$ with absolute magnitude for different mixing depths and mass-loss parameters. The groups of lines are labeled by the mixing depth, ΔX . The long-dashed, short-dashed, dotted and solid lines are for Reimers' (1975) $\eta = 0.6, 0.4, 0.2$ and 0.0 , respectively. The vertical dotted lines represents the low end of “high” $[\text{Al}/\text{Fe}]$ values in M 13.

according to the magnitudes at which the various mixing depths predict the aluminum abundances will cross the $[Al/Fe] = +0.4$ threshold. The results are shown in Table 8, where the first two columns describe the models and the next five discuss the data. The first column gives the mixing depth and the second column describes how far down the RGB the models predict a star will cross into the “high” aluminum group for that mixing depth, while the third column gives the fraction of stars in the bin (out of 96). The fourth and fifth columns give the P -value and the Al ratio for stars in the bin, respectively, while final two columns give the P -value and the Al ratio for the remaining stars outside the bin.¹².

If the assumption that mixing is the cause of the aluminum enhancements in the bright giants of M 13 holds, then it is apparent from Table 8 that it must turn on somewhere during the brightest magnitude of the RGB, as the Al ratio changes from 67:33 to 88:12 as one approaches the RGB tip. This signifies that at least 21% of the giants are experiencing deep mixing. We call this a lower limit because our technique for measuring aluminum enhancements cannot detect mixing in stars with initially high $[Al/Fe]$ values. Since two-thirds of the giants in M 13 appear to have high aluminum abundances before mixing takes effect, we could be missing a substantial number of stars undergoing deep mixing. If the same relative number of giants with initially high aluminum abundances undergo deep mixing as the relative number of giants with initially low aluminum abundances, the percentage of all stars undergoing deep mixing jumps to 63%.

5.4. Deep Mixing, the Blue-Tail Parameter and the Signatures of AGB Pollution

Deep mixing in red giants might have an effect on their future evolution. For example, Carretta & Gratton (1996) noticed a relationship between the HB morphology and the amount of depletion of oxygen in RGB stars. This does not necessarily imply that oxygen is a second parameter, but

¹²It must be emphasized again that the KMM algorithm is only accurate for sample sizes greater than 50; nonetheless, we include the P -values for the sake of completeness.

Table 8. Ratio of Al-enhanced to Al-normal Giants in M 13

| ΔX | ΔM_V from RGB tip | % Stars IN | P -value IN | Al Ratio IN | P -value OUT | Al Ratio OUT |
|------------|------------------------------|---------------|------------------|----------------|-------------------|-----------------|
| 0.05 | 0.50 | 18 | 0.005 | 7.5 ± 5.6 | 0.000 | 1.7 ± 0.2 |
| 0.10 | 1.00 | 35 | 0.000 | 2.8 ± 1.1 | 0.007 | 1.7 ± 0.5 |
| 0.15 | 1.30 | 44 | 0.001 | 2.5 ± 0.9 | 0.005 | 1.8 ± 0.5 |
| 0.20 | 1.50 | 46 | 0.001 | 2.4 ± 0.8 | 0.006 | 1.9 ± 0.6 |

rather that whatever is responsible for the oxygen depletions might also be causing the blueward shift in the HB. One such mechanism that can do both is rotation, which has several effects: 1) it can extend the life of a red giant, causing it to lose more mass and ultimately end up on the blue HB, 2) it can drive meridional circulation currents, which can deplete the oxygen, and 3) if fast enough, it can cause the circulation currents to penetrate the H shell and bring helium to the surface. This extra helium causes RGB stars to evolve to the blue HB at brighter luminosities than their unmixed counterparts, mimicking the second-parameter effect and reproducing the upward slope of the HB with decreasing color (Sweigart & Catelan 1998) that is observed in some metal-rich clusters (Piotto et al. 1997; Rich et al. 1997).

In this section, we examine the suggestion by Ferraro et al. (1998) that a so-called “blue-tail second parameter” (BTP) exists in M 13. Such a parameter differs from the more commonly sought after second parameter in the sense that the latter typically deals with difference in HB morphology on the flat part of the HB, whereas the former describes how clusters like M 13, M 80 and NGC 6752 develop extended blue tails. We attempt to discover whether or not deep mixing can be a/the BTP by adding extra helium into the atmosphere of RGB stars. Unfortunately, helium cannot be measured spectroscopically in cool giants; however, as shown in Figure 8, aluminum is made from magnesium inside the H shell where helium is being produced, so that the mixing of helium is accompanied by the mixing of aluminum; i.e., aluminum can be a good tracer of helium mixing. We conclude that if deep mixing is a BTP and if aluminum traces helium mixing, then there should exist a correlation between the Al ratio and the HB morphology. To describe the HB morphology quantitatively, we suggest using at the ratio of blue to red HB stars (hereafter, the “HB ratio”), which, of course, require definitions of their own. Perhaps a solution can be found in the corollary assumption that if cluster giants do not mix, then the cluster should not have an extended blue tail on the HB. Therefore, by assumption, a cluster like M 3, whose giants appear not to experience deep mixing, defines the “red” HB, so that for clusters like M 13, any star on the HB that is hotter than the M 3 HB is defined as “blue,” provided, of course, that the clusters are similar in all other ways (e.g., metallicity, age, environment, etc.).

To make the comparison between M 3 and M 13, we obtained high-quality Hubble Space Telescope photometric data for both clusters from Dr. F. Ferraro and shifted the M 3 HB by $\delta V = -0.6$ and $\delta(U - V) = -0.03$ to align it with that of M 13, as done by Ferraro et al. (1998). We then plotted histograms of the distributions of colors along the HB’s for each cluster, as shown in Figure 14, and compared the HB ratio in M 13 with its Al ratio. We define stars with $U - V < -0.3$ as being blue, which gives a HB ratio of 58:42. We note that while this choice of color coincides with the apparent gap in Figure 14, it is chosen because this is where the M 3 distribution drops off and not because of the appearance of bimodality in the M 13 distribution. To estimate an error in the HB ratio, we fit a Gaussian to the M 3 distribution to determine the standard deviation, σ , and call blue all M 13 stars hotter than the mean minus 3σ in M 3, resulting in an HB ratio of 74:26. Compared with the 21% to 63% deeply mixed stars on the RGB, the 58% to 74% blue HB stars is consistent with deep mixing as the BTP; although, the uncertainties in the

number of RGB stars that have undergone deep mixing makes the results less robust than desired.

It would be helpful if we could discriminate between stars that have undergone deep mixing and those that have been polluted. One way to do this might be by using the *s*-process abundances, which are also created in intermediate-mass AGB stars (IMS) with aluminum, albeit at different locations within the stars (Denissenkov et al. 1998; Lattanzio 1999; Boothroyd & Sackmann 1999). Stars above $M \gtrsim 4 M_{\odot}$ experience HBB, which, as discussed above, result in the production of ^{27}Al from magnesium. These same stars also create a neutron exposure during the thermal pulses in the He-burning shell that favors the production of the Sr-Y-Zr peak elements and ^{25}Mg , all through the $^{22}\text{Ne}(\alpha, n)^{25}\text{Mg}$ reaction (Gallino et al. 1999). If the *n*-rich material is mixed with the HBB by-products and ejected into the cluster medium, then one should trace the other in the polluted stars. Specifically, we expect stars with high *s*-process abundances to also have high [Al/Fe] values, but not vice-versa. The key is to choose the best *s*-process elements that trace the Al-rich IMS ejecta. We suggest using zirconium since many lines are available in the optical spectrum and it's abundance easily computed (Cavallo & Nagar 2000). Conversely, elements near the barium peak would not be good choices to represent the *s*-process/HBB enhancement from IMS since they are produced in low-mass AGB stars ($M \sim 2 M_{\odot}$).

5.5. On the Overproduction of Sodium

Recently, Charbonnel et al. (1999) pointed out that mixing into the H shell to enrich the stellar atmosphere in aluminum and helium would result in an overproduction of sodium by $\gtrsim 0.3$ dex (see their Figure 3) relative to the M 13 data, essentially precluding deep mixing. This constraint keeps the change in the atmospheric helium abundance to less than 0.06, much less than the 0.20 found by Sweigart (1997a,b) that is needed to account for the most extended HB's seen in clusters like M 13. We submit that the solution to this discrepancy might be found in the initial abundances; i.e., primordial contamination from the IMS plays a role. Our algorithm shows that the overproduction of sodium is avoided, even with deep mixing, if the initial ^{22}Ne abundance were depleted as a result of $^{22}\text{Ne}(\alpha, n)^{25}\text{Mg}$ reaction in the IMS, which also enhances the initial ^{25}Mg , as needed to produce the large aluminum enhancements in the RGB stars. The calculations of Gallino et al. (1999) indicate that the ^{22}Ne abundance is depleted by approximately 30% during the thermal pulses in IMS, but it is not clear how HBB and interpulse burning affects the net ^{22}Ne abundance. One would assume that HBB would deplete the ^{22}Ne reserves in the convective envelope and produce ^{23}Na as is done on the RGB. In contradistinction, the AGB yields calculated by Denissenkov et al. (1998) actually enhance the net ^{22}Ne abundance from a series of α captures on ^{14}N . Clearly, a more complete and detailed look into the yields of all abundances from primordial AGB stars is necessary to determine a more translucent picture of how pollution plays a role on the RGB.

Our hypothesis is consistent with the sodium data, which raise two important questions: 1) why does the Na ratio increase only at the same magnitudes as the Al ratio when sodium is very easily produced from ^{22}Ne above the H shell at luminosities far below the RGB tip, and 2) why does

the sodium abundance vary without oxygen abundance variations for “oxygen-normal” giants (see, e.g., KSLP). The answer to both these questions might be found on the AGB: if ^{22}Ne is depleted to build up ^{25}Mg during the He-shell flashes and ^{23}Na during HBB, then sodium will not be produced at lower magnitudes on the RGB, but will be made at brighter magnitudes from ^{20}Ne with deep mixing. The extra sodium produced during HBB could be distributed locally within the cluster creating the [Na/Fe]-rich stars that are independent of their oxygen abundances. Although oxygen is likely depleted during HBB, this is unlikely to create an oxygen-poor RGB atmosphere since it is easier to enhance elements in an atmosphere than to deplete them by pollution. A primordial pollution scenario is consistent with the data that show aluminum and sodium enhancements on the lower RGB and, for some clusters, on the main sequence and subgiant branch, and can help prevent the overproduction of sodium during deep mixing.

6. CONCLUSIONS

Before we discuss our final conclusions, we first remind the reader of the number of assumptions that have gone into our analysis. First, there are errors associated with the abundance determinations that we tried to characterize by allowing for significant variations in the model atmosphere parameters, which contribute the most to the uncertainty in the analysis. Second, the inclusion of the WIYN data into our analysis comes at a price: the data have poor signal-to-noise ratios, come from only one line and require the assumption that, for some stars with indeterminate line strengths, the [Al/Fe] value is “low.” Third, despite that fact that this is the largest compilation of [Al/Fe] and [Na/Fe] values in one globular cluster to be analyzed in a single paper, the data are still subject to small number effects, particularly at the RGB tip. Unfortunately, there are only so many tip stars that can be spectroscopically measured from the ground, leaving this problem difficult to solve. We suggest the best way to handle the small numbers is to expand this analysis to other clusters for a broad comparative study. Fourth, the models have many assumptions in them: we assume that canonical evolution holds and add in our mixing algorithm after the fact, we assume that mixing is instantaneous, we assume that the abundances are distributed as per Denissenkov et al. (1998), we assume that our reaction rates are accurate, and we assume that we adequately searched the parameter space allowed by the uncertainties in the initial abundances, nuclear reaction rates and mass-loss rates. Fifth, we assume that no other second parameter affects the relationship between the M 3 and M 13 HB morphologies. Sixth, we make no attempt to correct for blending of the AGB with the RGB when performing our analysis. Approximately 20% of the red giants above the point where giant branches merge are supposedly AGB interlopers based on comparative lifetimes: the problem is to determine which ones are really AGB stars. This might not be as much of a problem for the M 13 sample, however, since blue HB stars tend to evolve away from the AGB. The best workaround for this problem is also an extension of our analysis to other clusters to look for consistent trends despite this, and the other, uncertainties.

The importance of having accurate nuclear reaction rates cannot be overstated. This is partic-

ularly true when using aluminum as a diagnostic of deep mixing. If we were to vary, for example, the ^{26}Mg proton-capture rate to its upper limit in range of $T_9 = 0.05 - 0.06$, the production of Al can move outside the H shell, although, just barely. Depending on the initial abundances of ^{25}Mg and ^{26}Mg , this might be able to account for the full enhancements of aluminum that we observed. In addition, according to the NACRE compilation, the rate for $^{26}\text{Al}^9(p, \gamma)^{27}\text{Si}$ is uncertain by as much as three orders of magnitude in the same temperature range. Increasing these rates might help solve the problem presented by Charbonnel et al. (1999) who show that, if mixing occurs below the top of the H shell, sodium is overproduced due to the extra enhancement from ^{20}Ne in the NeNa cycle, a result we confirm with our instantaneous mixing algorithm. If the ^{26}Mg proton-capture rate is near its upper limit, then deep mixing is not required to produce the observed aluminum abundances and sodium is not over enhanced compared to the observations.

Our general results for the M 3 and M 13 abundances obtained in this work show the usual trends in the proton-capture, α and iron-peak elements: the sodium and aluminum abundances are anticorrelated with oxygen, the α elements are enhanced by approximately 0.3 dex and the iron-peak elements remain constant.

Our analysis shows that the variation in both the [Al/Fe] and [Na/Fe] ratios are consistent with deep mixing occurring on the RGB in M 13 and not in M 3. The aluminum and sodium data are correlated for the M 13 giants; although, the Al ratio is probably a better indicator of deep mixing since it is more easily separated into “high” and “low” groups. We would not expect such a similar tight correlation between aluminum and sodium in the M 3 giants since sodium can be enhanced without increasing the aluminum abundance if the mixing currents do not penetrate the H shell, as seems indicated in M 3 from the low Al ratio. However, some semblance of a correlation between aluminum and sodium might be set up by primordial effects in this cluster. In addition, the Na ratio increases near the same magnitude as the Al ratio, which is contrary to the previous predictions that sodium should be enhanced further down the RGB from ^{22}Ne (CSB98). Our models show that this would be expected if the ^{22}Ne were depleted in primordial intermediate-mass AGB stars.

When comparing the Al ratio with the HB ratio, it seems that the assumption of deep mixing as a blue-tail parameter is self-consistent; however, the large range allowed in the actual number of mixed RGB stars and the empirical definitions of “blue” and “red” HB stars do not constrain the results enough to be firmly conclusive. Again we suggest that a similar analysis as the one presented here be extended to other clusters to determine the Al ratio as a function of V and to compare this with the HB ratio. If the Al ratio at the RGB tip can be shown to be a predictor of the HB ratio, then helium mixing would certainly be given greater credence as a blue-tail second parameter, supplanting the oft-assumed cluster age differences that have been shown to fail for this classical pair of clusters. In particular, we suggest the study of metal-rich clusters to see if the aluminum distribution is bimodal, and if it is, if the Al ratio varies. According to our models, it should not vary since aluminum cannot be produced in metal-rich cluster giants on the same scale as it can in the intermediate metallicity and metal-poor giants. In addition, we suggest further examination of the sodium abundance in clusters to search for similar behavior as in M 13. Also,

we suggest a more extensive comparison of the *s*-process abundances with the aluminum data as a test of primordial contamination.

Finally, we conclude that the problem of abundance anomalies in globular cluster red giants requires detailed study of the abundance yields from primordial AGB stars as well as an in-depth and complete study of the hydrodynamical evolution of rotating RGB stars. In the meantime, aluminum, and to a lesser extent, sodium, give the best diagnostics of deep mixing during the evolution up the RGB and the *s*-process elements near the Sr-Y-Zr peak are the best tracers of AGB pollution from IMS.

The authors expressly acknowledge and thank Caty Pilachowski for allowing us to use her data and for her valuable help in analyzing them. We also extend our gratitude to Mike Briley, who supplied us with the unpublished data for the star M 3 AA and who acted as our referee with many thoughtful and valuable comments. We thank Bob Kraft and Chris Sneden, who sent us their original Lick spectra for the stars in common between our two studies, and to Michael Bolte, who provided us with finding charts for the star MB 4. We express our gratitude to Francesco Ferraro for making his recent HB photometry for M 13 and M 3 available to us. We thank Carrie Rowland for giving us updated data for the ^{26}Mg proton capture rates and we look forward to her experimental results regarding this reaction. Our thanks are given to Keith Ashman for supplying us with a FORTRAN version of his KMM algorithm. In addition, we are indebted to Roger Bell for providing us with his latest isochrones describing color- T_{eff} relations. We also thank Allen Sweigart for his many invaluable discussions throughout the development of this project. We wish to thank Daryl Wilmarth for his aid in gathering and reducing the data and Frank Hill for providing us with the Kitt Peak solar spectrum. We likewise acknowledge Jennifer Johnson and Peter Stetson for making their separate photometric data sets available to us. N. M. N. acknowledges travel support from the Astronomy Department at UMD and R. M. C acknowledges KPNO for travel support while he was a visiting graduate student. This work was performed while R. M. C. held a National Research Council-GSFC Research Associateship. Funding for publication was provided in part by a Small Research Grant from the American Astronomical Society.

A. INSTANTANEOUS MIXING ALGORITHM

This derivation of instantaneous mixing begins with the form of the nuclear reaction equation that involves the proton-capture reactions and β -decays; although, it is easily extended to other rates and is applied in its most general form in our code:

$$\frac{dn_i}{dt} = \sum_j (\pm n_j n_{\text{H}} \langle \sigma v \rangle_j \pm n_j \frac{\ln 2}{\tau_j}), \quad (\text{A1})$$

where n_i is the number of nuclei of type i cm^{-3} that are being produced or destroyed, n_j is the number cm^{-3} of nuclei that produce (+ sign) or, when $j = i$, destroy (– sign) nuclei of type i , n_{H}

is the number cm^{-3} of protons, $\langle \sigma v \rangle_j$ is the velocity-averaged cross section of the proton-capture reaction and τ_j is the mean lifetime of radioactive isotopes that destroy or produce element i .

If we integrate equation A1 over a mass interval from some mixing depth, M_d , to the surface, M , and substitute the molar fraction $Y = n/\rho N_A$, where ρ is the density and N_A is Avogadro's number, so that $Y_H = X$, the hydrogen-mass fraction, we get

$$\int_{M_d}^M \frac{dY_i}{dt} dM_r = \sum_j (\pm \int_{M_d}^M Y_j X N_A \langle \sigma v \rangle_j \rho dM_r \pm \frac{\ln 2}{\tau_j} \int_{M_d}^M Y_j dM_r), \quad (\text{A2})$$

which is equivalent to spreading the nuclearly processed material over the whole mixing zone. Mass loss can be accounted for by modifying the total integrated mass by some mass-loss recipe such as given by Reimers (1975).

Now assuming that the mixing is instantaneous so that dY_i/dt , Y_j and X vary little over the whole mixing zone, we can rewrite equation A2 as

$$\frac{dY_i}{dt} \int_{M_d}^M dM_r = \sum_j (\pm Y_j X \int_{M_d}^M N_A \langle \sigma v \rangle_j \rho dM_r \pm \frac{\ln 2}{\tau_j} Y_j \int_{M_d}^M dM_r). \quad (\text{A3})$$

The first integral on the right hand side is just the mass-averaged reaction rate that can be substituted as an effective reaction rate, $\langle \sigma v \rangle_j^{\text{eff}}$, while the other two integrals in equation A3 are just the total mixed mass, M_{mix} . Thus, equation A3 can now be written

$$\frac{dY_i}{dt} = \frac{1}{M_{\text{mix}}} \sum_j (\pm Y_j X \langle \sigma v \rangle_j^{\text{eff}} \pm \frac{\ln 2}{\tau_j} Y_j), \quad (\text{A4})$$

the final form of equation A1 under the assumptions of instantaneous mixing.

The implementation of this equation in our nuclear reaction network is straightforward. We average the reaction rates together by weighting the reaction rate determined at each mesh point by the mass contained between that mesh point and the one below it and summing over all the mass intervals. The temperature and density for calculating the reaction rate for each mass interval are taken at the top mesh point (towards the surface). Since the spacing between mesh points becomes closer as the temperature profile steepens, the differences between the temperature and density at the top and bottom of the mass intervals has negligible influence on the effective reaction rates. The effective rates are then applied to the initial abundances and integrated ("mixed") over some determined mass interval where the mixing depth and mass-loss rate are the free parameters chosen by the user. The burning timescale is controlled by limiting how much the fastest changing isotope with some chosen minimum abundance can vary in a single timestep. New models are interpolated from a sequence at timesteps according to this nuclear burning timescale. Each new model contains the output abundances derived from the previous model for its input abundances. The mixing algorithm can begin anywhere on the RGB and proceeds until the helium flash is encountered at the tip. The code outputs the new abundances, the mass-averaged reaction rates and information regarding the position of the model on the theoretical RGB.

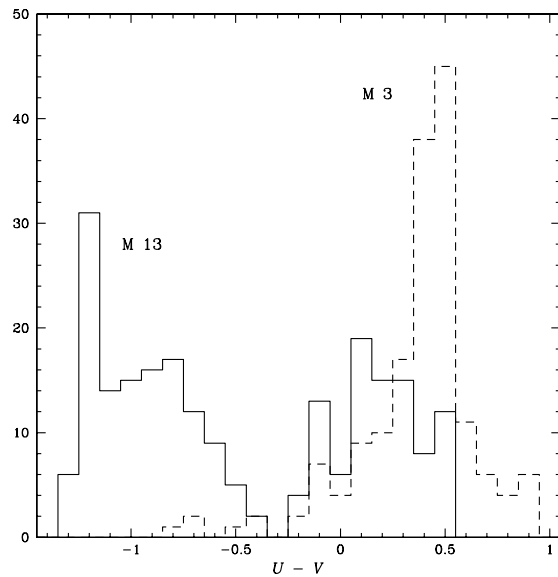


Fig. 14.— Histograms of the HB distributions in M 3 (dashed line) and M 13 (solid line). The photometry is from Ferraro et al. (1998) and the M 3 data have been shifted by $\delta V = -0.6$ and $\delta(U - V) = -0.03$.

REFERENCES

Anders, E. & Grevesse, N. 1989, *Geochim. Cosmochim. Acta*, 53, 197

Angulo, C. et al. 1999, *Nucl. Phys. A*, A656, 3

Armosky, B. J., Sneden, C., Langer, G. E. & Kraft, R. P. 1994, *AJ*, 108, 1364

Arp, H. C. 1955, *AJ*, 60, 317

Ashman, K. M., Bird, C. M. & Zepf, S. E. 1994, *AJ*, 108, 2348

Bell, R. A., Dickens, J. A. & Gustafsson, B. 1979, *ApJ*, 229, 604

Biémont, E., Baudoux, M., Kurucz, R. L., Ansbacher, W. & Pinnington, E. H. 1991, *A&A*, 249, 539

Blackwell, D. E., Lynas-Gray, A. E. & Smith, G. 1995a, *A&A*, 296, 217

Blackwell, D. E., Smith, G. & Lynas-Gray, A. E. 1995b, *A&A*, 303, 575

Boothroyd, A. I. & Sackmann, I.-J. 1999, *ApJ*, 510, 232

Briley, M. M., Bell, R. A., Smith G. H. & Hesser, J. E. 1989, *ApJ*, 341, 800

Briley, M. M., Bell, R. A., Hesser, J. E. & Smith, G. H. 1994, *Can. J. Phys.*, 72, 772

Briley, M. M., Bell, R. A., Hoban, S. & Dickens, R. J. 1990, *ApJ*, 359, 307

Briley, M. M., Grundahl, F. & Andersen, M. I. 1999, *BAAS*, 195, 3.03

Briley, M. M., Hesser, J. E & Bell, R. A. 1991, *ApJ*, 373, 482

Briley, M. M., Smith, V. V., King, J., & Lambert, D. L. 1997a, *AJ*, 113, 306

Briley, M. M., Smith, V. V., Suntzeff, N. B., Lambert, D. L., Bell, R. A. & Hesser, J. E. 1996, *Nature*, 383, 604

Briley, M. M., Suntzeff, N. B., Smith, V. V., Bell, R. A., & Norris, J. 1997b, *BAAS*, 189, 1363

Cannon, R. D., Croke, B. F. W., Bell, R. A., Hesser, J. E. & Stathakis, R. A. 1998, *MNRAS*, 298, 601

Carbon, D. F. 1982, *ApJS*, 49, 207

Carretta, E. & Gratton, R. G. 1996, in *Formation of the Galactic Halo...Inside and Out*, eds. H. Morrison and A. Sarajedini (ASP: San Francisco), p. 359

Carretta, E., Gratton, R. G., Sneden, C. & Bragaglia A. 1999, in *The Chemical Evolution of the Milky Way: Stars vs Clusters*, eds. F. Matteuci and F. Giovanelli, in press

Caughlin, G. R. & Fowler, W. A. 1988, *Atomic Data and Nuclear Data Tables*, 40, 283

Cavallo, R. M. 1998a, Ph. D. Thesis, University of Maryland

Cavallo, R. M. 1998b, in *Stellar Evolution, Stellar Explosions and Galactic Chemical Evolution*, ed. Anthony Mezzacappa (Inst. of Physics: Bristol), p. 357

Cavallo, R. M. & Nagar, N. M. in prep.

Cavallo, R. M., Sweigart, A. V. & Bell, R. A. 1996, ApJ, 464, L79

Cavallo, R. M., Sweigart, A. V. & Bell, R. A. 1998, ApJ, 492, 575

Chaboyer, B., Demarque, P., Kernan, P. J. and Krauss, L. M. 1998, ApJ, 494, 96

Charbonnel, C. 1994, A&A, 282, 811

Charbonnel, C. 1995, ApJ, 453, 811

Charbonnel, C., Denissenkov, P. A. & Weiss, A. 1999, to appear in The Galactic Halo – From Globular Cluster to Field Stars (astro-ph/9909440)

Cohen, J. G., Frogel, J. A. & Persson, S. E. 1978, ApJ, 222, 165

Cottrell, P. L. & Da Costa, G. S. 1981, ApJ, 245, L79

Cudworth, K. M. & Monet, D. G. 1979, AJ, 84, 774

Denissenkov, P. A., Da Costa, G. S., Norris, J. E. & Weiss, A. 1998, A&A, 333, 926

Denisenkov, P. A. & Denisenkova, S. N. 1990, Sov. Astron. Lett., 16, 275

Denissenkov, P. A., Weiss, A. & Wagenhuber, J. 1997, A&A, 320, 115

Denissenkov, P. A. & Weiss, A. 1996, A&A, 308, 773

Ferraro, F. R., Carretta, E., Corsi, C. E., Fusi Pecci, F., Cacciari, C., Buonanno, R., Paltrinieri, B. & Hamilton, D. 1997, A&A, 320, 757

Ferraro, F. R., Paltrinieri, B., Fusi-Peccci, F., Rood, R. T. & Dorman, B. 1998, ApJ, 500, 311

Fujimoto, M. Y., Aikawa, M. & Kato, K. 1999, ApJ, 519, 733

Fusi Pecci, F. & Bellazini, M. 1997, in The Third Conference on Faint Blue Stars, eds. A. G. D. Philips, J. W. Liebert and R. A. Saffer (L. Davis: Schenectady), p. 255

Fusi Pecci, F., Ferraro, F. R., Crocker, D. A., Rood, R. T. & Buonanno, R. 1990, A&A, 238, 95

Gallino, R., Busso, M., Lugaro, M., Travaglio, C. & Straniero, O. 1999, to appear in Proc. of 35th Liege International Astrophysics Colloquium, eds. A. Noels et al., in press

Gilroy, K. K. & Brown, J. A. 1991, ApJ, 371, 578

Grundahl, F. G. 1999, in Spectrophotometric Dating of Stars and Galaxies, eds. I. Hubeny, S. R. Heap and R. H. Cornett (ASP: San Francisco). p. 223

Gustafsson, B., Bell, R. A., Eriksson, K. & Nordlund, Å. 1975, A&A, 42, 407

Hogg, H. S. 1973, Publ. David Dunlap Obs., 3, No. 6

Holweger, H., Kock, M. & Bard, A. 1995, A&A, 296, 233

Holweger, H. & Müller, E. A. 1974, *Sol. Phys.*, 39, 19

Iben, I. Jr. 1967, *ApJ*, 147, 634

Ivans, I. I. et al. 1999, *AJ*, 118, 1273

Johnson, J. A. & Bolte, M. 1998, *AJ*, 115, 693

Kostik, R. J., Shchukina, N. G. & Rutten, R. J. 1996, *A&A*, 305, 325

King, J. R., Stephens, A. & Boesgaard, A. M. 1998, *AJ*, 115, 666

Kraft, R. P. 1994, *PASP*, 106, 553

Kraft, R. P., Sneden, C., Langer, G. E. & Prosser, C. F. 1992, *AJ*, 104, 645

Kraft, R. P., Sneden, C., Langer, G. E. & Shetrone, M. D. 1993, *AJ*, 106, 1490

Kraft, R. P., Sneden, C., Langer, G. E., Shetrone, M. D. & Bolte, M. 1995, *AJ*, 109, 2586

Kraft, R. P., Peterson, R. C., Guhathakurta, P., Sneden, C., Fulbright, J. P. & Langer, G. E. 1999 *ApJ*, 518, L53

Kraft, R. P., Sneden, C., Smith, G. H., Shetrone, M. D., Langer, G. E. & Pilachowski, C. A. 1997, *AJ*, 113, 279

Langer, G. E., Hoffman, R. & Sneden, C. 1993, *PASP*, 105, 301

Langer, G. E., Hoffman, R. D., & Zaidins, C. S. 1997, *PASP*, 109, 244

Langer, G. E., Kraft, R. P., Carbon, D. F. Friel, E. 1986, *PASP*, 98, 473

Lattanzio, J. C. 1999, in *Proceedings of Nuclei in the Cosmos V*, eds. N. Orantzos and S. Harissopoulos, (Editions Frontieres), p 163

Lattanzio, J., Forestini, M. & Charbonnel, C. 1999, to appear in *The Changes in Abundances in Asymptotic Giant Branch Stars* (astro-ph/9912298)

Lehnert, M. D., Bell, R. A., & Cohen, J. G. 1991, *ApJ*, 367, 514

Ludendorf 1905, *Publ. Astrophys. Obs. Potsdam*, 15, No. 50

Moore, C. E., Minnaert, M. G. J. & Houtgast, J. 1966, *The Solar Spectrum 2935Å to 8770Å*, 2nd Ed., (Washington, D.C.: National Bureau of Standards)

Nave, G., Johansson, S., Learner, R. C. M., Thorne, A. P. & Brault, J. W. 1994, *ApJS*, 94, 221

Peterson, R. C. 1983, *ApJ*, 275, 737

Pilachowski, C. A., Sneden, C., Kraft, R. P., Harmer, D. & Willmarth, D. 2000, *AJ*, in press

Pilachowski, C. A., Sneden, C., Kraft, R. P., & Langer, G. E. 1996, *AJ*, 112, 545

Piotto, G. et al. 1997, in *Advances in Stellar Evolution*, ed. R. T. Rood and A. Renzini (Cambridge: Cambridge Univ. Press), p 84

Powell, D. C., Iliadis, C., Champagne, A. E., Grossman, C. A., Hale, S. E., Hansper, V. Y. & McLean, L. K. 1999, *Nucl. Phys. A*, 660, 349

Reimers, D. 1975, in *Mémoires de la Société Royale des Sciences de Liège*, 6e serie, tome VIII, *Problèmes D'Hydrodynamique Stellaire*, p. 369

Rich, R. M. et al. 1997, *ApJ*, 484, L25

Sandage, A. R. 1953, *AJ*, 58, 61

Sandage, A. & Karem, B. 1982, *AJ*, 87, 537

Sarajedini, A., Chaboyer, B. & Demarque, P. 1997, *PASP*, 109, 1321

Shetrone, M. D. 1996a, *AJ*, 112, 1517

Shetrone, M. D. 1996b, *AJ*, 112, 2639

Shetrone, M. D. 1997, in *Poster Proc of IAU Symp. 189: The Interaction between Observations and Theory*, ed. T. R. Bedding (Univ. of Sydney: Sydney), p. 158

Sneden, C. 1973, *ApJ*, 184, 839

Sneden, C., Kraft, R. P., Prosser, C. F. & Langer, G. E. 1991, *AJ*, 102, 2001

Suntzeff, N. B. 1981, *ApJS*, 41, 1

Suntzeff, N. B. & Smith, V. V. 1991, *ApJ*, 381, 160

Sweigart, A. V. 1997a, *ApJ*, 474, L23

Sweigart, A. V. 1997b, in *The Third Conference on Faint Blue Stars*, eds. A. G. D. Philips, J. W. Liebert and R. A. Saffer (L. Davis: Schenectady), p. 3

Sweigart, A. V. & Catelan, M. 1998, *ApJ*, 501, L63

Sweigart, A. V. & Mengel, J. G. 1979, *ApJ*, 229, 624

Taylor, J. R. 1982, *An Introduction to Error Analysis: The Study of Uncertainties in Physical Measurements*, ed. E. D. Commins (University Science Books: USA)

Thévenin, F. 1989, *A&AS*, 77, 137

Thévenin, F. 1990, *A&AS*, 82, 179

Tody, D. 1986, "The IRAF Data Reduction and Analysis System" in *Proc. SPIE Instrumentation in Astronomy VI*, ed. D.L. Crawford, 627, 733

Trefzger, C. F., Carbon, D. F., Langer, G. E., Suntzeff, N. B. & Kraft, R. P. 1983, *ApJ*, 266, 144

VandenBerg, D. A. 1999, in The Third Stromlo Symposium: The Galactic Halo, eds. B. K. Gibson, T. S. Axelrod and M. E. Putnam (San Francisco :ASP) p. 46

Von Rudloff, I. R., VandenBerg, D. A. & Hartwick, F. D. A. 1988, *ApJ*, 324, 840

von Zeipel, M. H. 1908, *Ann. Obs. Paris*, 25, F1

Wallace, L., Hinkle, K. & Livingston, W. 1993, N. S.). Technical Report #93-001

Wallace, L., Hinkle, K. & Livingston, W. 1998, N. S.). Technical Report #98-001

Wallerstein, G., Leep, E. M., & Oke, J. B. 1987, *AJ*, 93, 1137

Zaidins, C. S. & Langer, G. E. 1997, *PASP*, 109, 252

Zucker, D., Wallerstein, G., & Brown, J. A. 1996, *PASP*, 108, 911

Table 2. Measured Equivalent Widths (mÅ)

| Wavelength (Å) | E. P. (eV) | log (gf) | M 3 Giants | | | | | M 13 Giants | | | |
|-------------------|---------------|------------|------------|--------|--------|---------|---------|-------------|-------|-------|--------|
| | | | AA | vZ 297 | III-28 | vZ 1000 | vZ 1127 | MB 4 | L 262 | L 324 | III-56 |
| Na I | | | | | | | | | | | |
| 6154.23 | 2.10 | −1.66 | 33.5 | 20.7 | ... | ... | ... | 34.1 | 20.0 | 34.5 | 29.1 |
| 6160.75 | 2.10 | −1.32 | 51.7 | 29.8 | ... | 33.2 | 14.9 | 52.1 | 38.6 | 53.1 | 48.9 |
| Mg I | | | | | | | | | | | |
| 5711.09 | 4.35 | −1.58 | 110.7 | 93.2 | 73.9 | 93.8 | 83.5 | 96.4 | 91.5 | 87.2 | 100.4 |
| 8717.83 | 5.93 | −0.96 | ... | ... | ... | 18.8 | 15.7 | 21.5 | 11.9 | 10.4 | 18.4 |
| 8736.02 | 5.95 | −0.04 | ... | 59.1 | 50.7 | 74.0 | 54.1 | 68.2 | 51.6 | 45.5 | 52.7 |
| Al I | | | | | | | | | | | |
| 6696.03 | 3.14 | −1.54 | 69.0 | 52.4 | ... | 51.1 | 13.2 | 58.8 | 41.1 | 71.1 | 52.8 |
| 6698.67 | 3.14 | −1.91 | 40.1 | 24.6 | ... | 25.9 | 5.1 | 34.5 | 18.2 | 36.9 | 23.7 |
| 7835.31 | 4.02 | −0.72 | 36.0 | 28.3 | ... | 26.3 | ... | 31.3 | 18.3 | 38.7 | 23.4 |
| 7836.13 | 4.02 | −0.63 | 50.9 | 36.3 | ... | 30.2 | ... | 45.8 | 24.2 | 47.3 | 32.7 |
| 8772.86 | 4.02 | −0.35 | 63.1 | 60.1 | ... | 59.8 | ... | 64.0 | 38.0 | 80.1 | 51.2 |
| 8773.90 | 4.02 | −0.15 | 91.3 | 83.8 | ... | 81.0 | ... | 98.1 | 62.1 | 98.8 | 62.2 |
| Si I | | | | | | | | | | | |
| 6142.48 | 5.62 | −1.53 | 10.2 | ... | ... | ... | ... | 6.1 | 11.4 | 9.3 | 6.2 |
| 6145.02 | 5.61 | −1.41 | ... | ... | ... | ... | ... | ... | ... | 10.1 | 9.9 |
| 6243.82 | 5.61 | −1.32 | 17.1 | 14.8 | 11.7 | 16.7 | 14.0 | 15.4 | 15.3 | 11.9 | ... |
| 6721.85 | 5.86 | −1.16 | ... | ... | 9.0 | 14.0 | 12.3 | ... | 14.5 | 9.3 | 13.4 |
| 7405.77 | 5.61 | −0.57 | ... | 60.2 | 50.0 | 53.2 | 45.6 | 42.0 | ... | 55.0 | 41.7 |
| 7415.95 | 5.68 | −0.77 | ... | 44.7 | 31.5 | 43.6 | 33.4 | 28.6 | 45.2 | 36.8 | 34.6 |
| 8648.47 | 6.21 | −0.10 | 47.9 | ... | ... | ... | ... | ... | ... | ... | ... |
| 8742.45 | 5.87 | −0.41 | ... | 41.6 | 45.3 | 45.0 | 38.0 | 42.0 | ... | 41.1 | 36.3 |
| 8752.01 | 5.87 | −0.42 | ... | 56.2 | 36.2 | 47.4 | 47.4 | 35.8 | 54.1 | 47.2 | 37.9 |
| Ca I | | | | | | | | | | | |
| 6161.30 | 2.52 | −1.22 | 87.7 | 88.0 | 70.5 | 78.2 | 78.5 | 91.8 | 69.9 | 78.4 | 85.8 |
| 6166.44 | 2.52 | −1.04 | 95.5 | 90.1 | 64.6 | ... | 74.6 | 96.2 | 74.5 | 83.3 | 78.1 |
| 6169.04 | 2.52 | −0.67 | 115.9 | 112.5 | ... | 108.0 | 96.7 | 113.8 | 96.3 | 115.7 | 113.1 |
| 6439.08 | 2.53 | 0.26 | 197.3 | 182.1 | 166.7 | 176.5 | 169.3 | 182.9 | 166.7 | 196.8 | 185.8 |
| 6455.60 | 2.52 | −1.34 | 78.4 | 71.6 | 52.5 | 62.9 | 61.2 | 74.7 | 57.6 | 64.8 | 68.5 |
| 6471.66 | 2.53 | −0.67 | 123.1 | 113.5 | 99.2 | 112.9 | 102.2 | 123.8 | 108.3 | 131.0 | 120.3 |
| 6493.78 | 2.52 | −0.22 | 162.3 | 153.6 | 128.6 | 145.9 | 132.0 | 159.7 | 129.4 | 163.6 | 152.7 |
| 6499.65 | 2.52 | −0.79 | 119.7 | 103.0 | 96.4 | 105.0 | 91.8 | 109.7 | 89.3 | 107.8 | 104.4 |

Table 2—Continued

| Wavelength (Å) | E. P. (eV) | log (gf) | M 3 Giants | | | | | M 13 Giants | | | |
|-------------------|---------------|------------|------------|--------|--------|---------|---------|-------------|-------|-------|--------|
| | | | AA | vZ 297 | III-28 | vZ 1000 | vZ 1127 | MB 4 | L 262 | L 324 | III-56 |
| Ti I | | | | | | | | | | | |
| 5866.45 | 1.07 | −0.82 | 154.8 | 137.2 | 110.1 | 115.4 | 113.9 | 144.5 | 112.8 | 156.0 | 131.9 |
| 6064.63 | 1.05 | −1.99 | 72.4 | 58.0 | 36.3 | 42.9 | 38.0 | ... | 40.0 | 65.3 | 59.1 |
| 6126.22 | 1.07 | −1.43 | 113.9 | 95.4 | 75.3 | 77.6 | 84.8 | 108.9 | 81.2 | 104.0 | 93.2 |
| 6258.10 | 1.44 | −0.37 | 149.1 | 140.9 | 99.9 | 115.8 | 115.3 | 156.6 | 109.9 | 162.7 | 136.4 |
| 6261.10 | 1.43 | −0.46 | 159.1 | 138.4 | 96.9 | 119.6 | 114.4 | 147.4 | 108.4 | 154.9 | 136.2 |
| 6336.10 | 1.44 | −1.80 | 36.6 | 35.4 | 17.3 | 28.1 | 20.8 | 41.9 | 20.7 | 31.5 | 22.9 |
| 6497.68 | 1.44 | −2.10 | 29.5 | 13.0 | 13.5 | 10.8 | 14.0 | 28.6 | 11.1 | 19.8 | 14.3 |
| 6508.12 | 1.43 | −2.18 | 28.9 | 14.1 | 10.2 | 14.5 | 11.7 | 23.7 | 12.5 | 20.6 | 14.8 |
| Ti II | | | | | | | | | | | |
| 6219.94 | 2.06 | −3.14 | ... | ... | 9.7 | 9.2 | ... | 12.7 | 14.3 | 12.7 | 16.7 |
| 6491.56 | 2.06 | −2.07 | 75.1 | 63.5 | 63.0 | 65.9 | 66.4 | 61.7 | 66.3 | 72.0 | 71.8 |
| V I | | | | | | | | | | | |
| 5670.85 | 1.08 | −0.47 | 100.8 | 78.2 | 50.6 | 67.9 | 49.2 | 85.1 | 60.8 | 81.5 | 70.8 |
| 5727.05 | 1.08 | 0.02 | 142.4 | 120.3 | 80.2 | 105.3 | 99.9 | ... | 98.3 | 128.4 | 117.3 |
| 5727.65 | 1.05 | −0.92 | 68.8 | 50.0 | 23.8 | 35.6 | 32.7 | 53.3 | 35.6 | 47.2 | 49.5 |
| 5737.06 | 1.06 | −0.81 | 69.6 | 54.9 | 25.7 | 39.5 | 32.2 | 67.7 | 39.7 | 55.4 | 53.0 |
| 6039.72 | 1.06 | −0.73 | 70.7 | 57.0 | 33.4 | 43.7 | 49.3 | 64.0 | 45.0 | 61.0 | 60.3 |
| 6058.14 | 1.04 | −1.37 | 24.6 | 20.1 | ... | 12.4 | 12.8 | 26.3 | 14.5 | 16.8 | 15.7 |
| 6090.21 | 1.08 | −0.13 | ... | 96.7 | 69.7 | 90.0 | 76.3 | 107.2 | 82.1 | 103.0 | 96.4 |
| 6111.65 | 1.04 | −0.81 | 74.5 | 59.9 | 37.4 | 50.7 | 35.6 | 58.4 | 37.5 | 58.0 | 55.8 |
| 6150.16 | 0.30 | −1.56 | 102.6 | 84.5 | 40.6 | 58.8 | 58.8 | 98.7 | 59.8 | 90.1 | 77.7 |
| 6199.20 | 0.29 | −1.49 | ... | 112.3 | 57.1 | 88.6 | 76.3 | ... | 84.4 | 117.7 | 106.6 |
| 6224.53 | 0.29 | −1.89 | 80.5 | 64.4 | 28.9 | 43.0 | 40.6 | 70.5 | 50.2 | 68.7 | 60.6 |
| 6233.16 | 0.28 | −1.94 | 69.2 | 59.4 | 21.5 | 41.7 | 28.4 | 69.7 | 33.6 | 57.2 | 52.2 |
| 6251.83 | 0.29 | −1.40 | 127.6 | 101.6 | 57.4 | 80.4 | 76.0 | 119.9 | 80.6 | 108.0 | 96.3 |
| 6266.31 | 0.28 | −2.27 | 55.0 | 43.2 | 18.7 | 28.7 | 24.1 | 54.8 | 29.8 | 46.9 | 37.8 |
| 6274.65 | 0.27 | −1.76 | 95.6 | 79.0 | 40.9 | 53.1 | 44.5 | 83.4 | 51.9 | 82.8 | 74.2 |
| 6285.15 | 0.28 | −1.63 | 102.5 | 89.7 | 51.7 | 63.9 | 55.6 | 98.2 | 70.8 | 91.6 | ... |
| 6292.83 | 0.29 | −1.61 | 103.4 | 83.3 | 44.3 | 74.1 | 60.9 | 91.3 | 64.9 | 88.3 | 85.0 |
| 6531.42 | 1.22 | −0.97 | 44.7 | 33.0 | 17.2 | 25.3 | 20.3 | 41.8 | 23.8 | 32.4 | 32.0 |
| Mn I | | | | | | | | | | | |
| 6013.51 | 3.07 | −0.34 | 96.9 | 85.5 | 53.7 | 74.5 | 75.1 | 92.5 | 62.9 | 78.3 | 75.4 |
| 6016.67 | 3.07 | −0.24 | 94.7 | 101.9 | 63.5 | 73.5 | 74.2 | 88.3 | 77.1 | 85.7 | 84.3 |

Table 2—Continued

| Wavelength (Å) | E. P. (eV) | log (gf) | M 3 Giants | | | | | M 13 Giants | | | |
|-------------------|---------------|------------|------------|--------|--------|---------|---------|-------------|-------|-------|--------|
| | | | AA | vZ 297 | III-28 | vZ 1000 | vZ 1127 | MB 4 | L 262 | L 324 | III-56 |
| Fe I | | | | | | | | | | | |
| 6096.67 | 3.98 | −1.93 | 35.8 | 31.6 | 25.2 | 29.3 | 30.3 | 33.6 | 23.3 | 27.8 | 22.3 |
| 6127.91 | 4.14 | −1.40 | 42.1 | 42.7 | 40.6 | 34.3 | 45.6 | 45.0 | 34.5 | 37.4 | 32.7 |
| 6151.62 | 2.18 | −3.30 | 110.5 | 104.9 | 82.9 | 95.9 | 89.3 | 102.8 | 89.8 | 109.4 | 102.4 |
| 6157.73 | 4.07 | −1.26 | ... | 70.6 | 44.0 | 64.2 | 58.5 | ... | 57.3 | 70.0 | ... |
| 6165.36 | 4.14 | −1.47 | 42.4 | 35.8 | ... | 43.1 | 29.5 | 42.5 | 31.9 | 33.7 | 36.7 |
| 6187.99 | 3.94 | −1.72 | 50.2 | 45.6 | 34.0 | 39.6 | 32.4 | 39.1 | 38.3 | 43.7 | 40.6 |
| 6200.31 | 2.61 | −2.44 | ... | 125.6 | 108.6 | 111.5 | 112.4 | 118.4 | 106.1 | 131.9 | 113.8 |
| 6213.43 | 2.22 | −2.48 | 157.3 | 147.5 | 127.2 | 139.1 | 132.8 | 152.3 | 132.7 | 160.4 | 160.5 |
| 6219.28 | 2.20 | −2.43 | 164.7 | 149.0 | 136.0 | 147.2 | 137.0 | 161.2 | 136.3 | 171.5 | 158.1 |
| 6226.74 | 3.88 | −2.22 | 17.7 | 23.3 | 13.4 | 22.1 | ... | 21.7 | 19.6 | 21.1 | 16.7 |
| 6229.23 | 2.84 | −2.97 | 69.6 | 58.0 | 56.3 | 57.0 | 50.0 | 55.9 | 53.7 | 60.8 | 56.4 |
| 6246.32 | 3.60 | −0.88 | 133.5 | 118.9 | 115.6 | 111.6 | 124.5 | 123.2 | 114.3 | 126.5 | 124.0 |
| 6270.23 | 2.86 | −2.61 | 89.1 | 88.4 | 71.6 | 89.0 | 82.7 | 90.4 | 75.8 | 87.5 | 87.9 |
| 6297.80 | 2.22 | −2.74 | 152.3 | 129.2 | 116.2 | 117.6 | 120.2 | 131.5 | 121.5 | 156.4 | 142.2 |
| 6301.50 | 3.65 | −0.75 | 130.8 | 126.0 | 117.6 | 125.3 | 126.4 | 124.6 | 112.2 | ... | 123.9 |
| 6311.51 | 2.83 | −3.23 | ... | 51.6 | 37.5 | 50.6 | 44.1 | 52.7 | 39.7 | 50.6 | 34.9 |
| 6355.04 | 2.84 | −2.29 | 121.2 | 116.6 | 91.4 | 112.2 | 98.5 | 117.8 | 98.8 | 122.9 | 105.1 |
| 6380.75 | 4.19 | −1.38 | 51.9 | 48.3 | 32.0 | 42.8 | 35.3 | 48.1 | 42.5 | 47.2 | 38.8 |
| 6392.54 | 2.23 | −4.03 | 43.2 | 48.2 | 34.5 | 38.0 | 33.6 | 48.6 | 37.2 | 50.8 | 44.5 |
| 6393.60 | 2.43 | −1.58 | 196.4 | 191.5 | 166.8 | 182.0 | 171.3 | 206.3 | 187.0 | 222.5 | 183.0 |
| 6421.35 | 2.28 | −2.03 | 194.2 | 182.4 | 162.3 | 174.8 | 162.9 | 182.8 | 160.8 | 198.3 | 173.4 |
| 6430.85 | 2.18 | −2.01 | ... | 197.3 | 163.3 | 171.2 | 167.6 | 192.9 | 168.2 | 219.5 | 186.6 |
| 6495.74 | 4.84 | −0.94 | 16.7 | 17.8 | 16.5 | 16.0 | 20.1 | 20.5 | 13.3 | 15.8 | 15.3 |
| 6498.94 | 0.96 | −4.70 | 156.8 | 144.4 | 119.4 | 122.8 | 123.9 | ... | 122.9 | 163.3 | 136.9 |
| Fe II | | | | | | | | | | | |
| 5991.38 | 3.15 | −3.56 | 28.9 | 31.3 | 29.5 | 30.6 | 25.0 | 27.7 | 21.2 | 31.2 | 23.4 |
| 6149.25 | 3.89 | −2.72 | 22.0 | 23.3 | 21.0 | 21.3 | 21.6 | 20.4 | 19.7 | 23.6 | 21.6 |
| 6247.56 | 3.89 | −2.33 | 34.6 | 37.0 | 35.2 | ... | ... | 35.6 | 40.0 | 40.7 | 35.3 |
| 6369.46 | 2.89 | −4.25 | 12.1 | 16.0 | 13.2 | 17.3 | 15.8 | ... | 13.2 | 14.3 | ... |
| 6416.93 | 3.89 | −2.74 | 21.9 | 26.9 | 18.2 | 24.6 | 24.0 | 20.3 | 18.5 | 25.1 | 18.4 |
| 6432.68 | 2.89 | −3.71 | ... | 35.8 | 35.1 | 33.4 | 31.7 | 29.0 | 30.1 | 33.6 | 33.1 |
| 6456.39 | 3.90 | −2.08 | 47.3 | 53.0 | 49.1 | 58.0 | 49.3 | 48.1 | 51.9 | 57.8 | 44.6 |
| 6516.08 | 2.89 | −3.45 | 55.4 | 56.5 | 45.7 | 48.2 | 45.3 | 48.4 | 49.8 | 55.5 | 45.5 |

Table 2—Continued

| Wavelength (Å) | E. P. (eV) | log (gf) | M 3 Giants | | | | | M 13 Giants | | | |
|-------------------|---------------|------------|------------|--------|--------|---------|---------|-------------|-------|-------|--------|
| | | | AA | vZ 297 | III-28 | vZ 1000 | vZ 1127 | MB 4 | L 262 | L 324 | III-56 |
| Ni I | | | | | | | | | | | |
| 6086.28 | 4.27 | −0.39 | ... | 18.9 | 16.8 | 36.3 | 15.7 | 17.1 | 18.7 | 19.1 | 17.1 |
| 6108.11 | 1.68 | −2.44 | 137.0 | 115.8 | 90.7 | 106.7 | 102.2 | 124.0 | 107.7 | 133.0 | 120.5 |
| 6111.07 | 4.09 | −0.77 | 13.9 | 14.1 | ... | 23.0 | 18.0 | ... | 10.3 | 9.7 | 14.8 |
| 6175.36 | 4.09 | −0.45 | 29.3 | 33.4 | 17.6 | 21.8 | 26.7 | ... | 25.6 | 25.8 | 22.1 |
| 6176.81 | 4.09 | −0.13 | 43.8 | 42.7 | 35.0 | 33.4 | 34.4 | 50.5 | 37.2 | 38.0 | 35.8 |
| 6586.31 | 1.95 | −2.73 | 74.5 | 78.5 | 63.1 | 70.3 | 70.5 | 79.6 | 74.4 | 92.9 | 83.7 |
| 6643.63 | 1.68 | −1.85 | 169.9 | 157.5 | 138.7 | 155.9 | 145.9 | 169.1 | 143.5 | 179.0 | 160.6 |
| 6772.31 | 3.66 | −0.84 | 45.1 | 36.2 | 30.9 | 38.0 | 33.2 | 40.8 | 39.2 | 42.0 | 43.0 |
| 7525.11 | 3.64 | −0.53 | 65.7 | 67.1 | 57.6 | 63.5 | 64.6 | 72.7 | 71.2 | 73.0 | 70.8 |
| 7555.60 | 3.85 | 0.09 | ... | 85.2 | 72.6 | 77.9 | 72.0 | 81.3 | 75.7 | 95.3 | 82.5 |
| 7788.94 | 1.95 | −1.70 | 159.0 | 152.3 | 127.8 | 134.9 | 128.9 | 146.0 | 141.0 | 165.4 | 150.1 |
| 7797.59 | 3.90 | −0.14 | 74.6 | 70.4 | ... | 53.6 | 59.7 | 59.1 | 63.9 | 79.4 | 65.1 |